ARTICLES
https://doi.org/10.1038/s41929-020-00554-1
nature catalysis

Denary oxide nanoparticles as highly stable catalysts for methane combustion

Tangyuan Li[1,8], Yonggang Yao[1,8], Zhennan Huang[2,8], Pengfei Xie[3,8], Zhenyu Liu[4,8], Menghao Yang[1,8], Jinlong Gao[1], Kaizhu Zeng[3], Alexandra H. Brozena[1], Glenn Pastel[1], Miaolun Jiao[1], Qi Dong[1], Jiaqi Dai[1], Shuke Li[1], Han Zong[3], Miaofang Chi[5], Jian Luo[6], Yifei Mo[1], Guofeng Wang[4] ✉, Chao Wang[3] ✉, Reza Shahbazian-Yassar[2] ✉ and Liangbing Hu[1,7] ✉

Oxide nanoparticles with elemental and structural diversity are widely studied for catalysis and energy applications. While compositional control holds great promise for materials discovery, current oxide nanoparticles are typically limited to a few cations due to the intrinsic complexity in nanoscale multi-element mixing. Here we report the rational design and synthesis of single-phase multi-element oxide nanoparticles with tunable composition, size and structure. We have identified temperature-, oxidation- and entropy-driven synthesis strategies to mix a range of elements with largely dissimilar oxidation potentials (including palladium), thus greatly expanding the compositional space. Through rapid synthesis and screening, we obtained a denary multi-element oxide catalyst showing high performance and superior stability for catalytic methane combustion over 100 hours due to the high-entropy design and stabilization. Our work therefore provides a viable synthesis route with clear guidelines for multi-element oxide nanoparticles and enables materials design in the multi-element space towards highly stable catalysts.

Oxide nanoparticles[1,2] composed of three or more cations in a homogeneous phase, called multi-element oxide (MEO) nanoparticles, are promising for materials design and functional control as the synergistic interaction between different elements often outperforms unary oxides[3–5]. In addition, the multi-element mixing in MEO materials maximizes the configurational entropy and stabilizes the resultant structure even when this is applied in harsh environments[6–9]. For instance, in some preliminary reports, MEO structures (in bulk or powder form) have demonstrated improved performance and higher thermal stability in catalytic CO_2 hydrogenation and CO oxidation, and as battery cathode materials[10–12]. Since nanoscale materials have a much higher reactive surface and drastically reduced material cost, it is of great interest to develop MEO nanoparticles with tunable chemistry and structural durability for various applications, particularly as superior and stable catalysts.

However, previous reports of oxide nanoparticles have largely been limited to five or fewer cationic elements[13–16] due to the increased difficulty of mixing multiple dissimilar elements at the nanoscale[17]. Conventional wet-chemistry approaches (for example, solvothermal and co-precipitation)[18] performed at low temperatures (300–673 K) often lack the activation energy to overcome the kinetic barriers for mixing multiple elements, leading to phase separation in the oxide nanoparticles[19]. On the other hand, high-temperature sintering (for example, solid-state reactions and combustion)[20,21] features a higher activation energy and can promote multi-element mixing into a homogeneous phase, but is highly energy intensive and difficult to control for nanoscale particle formation[22,23]. Furthermore, according to the Ellingham diagram[24], metallic elements (from alkaline to noble metals) have a wide range of oxidation potentials at high temperature, which can easily lead to sequential phase separation or metallic impurities in a multi-element system (that is, failure of uniform mixing). Therefore, developing a general and reliable strategy for the controlled synthesis of diverse MEO nanoparticles is highly desirable and would provide more compositional options for enhancing the discovery of highly stable MEO catalysts through entropy stabilization.

In this work, we report the use of a rapid, non-equilibrium method for the synthesis of MEO nanoparticles with single-phase structure and uniform dispersion. The non-equilibrium synthesis features rapid high-temperature heating, which promotes multi-element mixing to form MEOs while the short heating duration effectively avoids particle aggregation and oxide reduction. Due to the large differences in the cations, we developed three strategies (temperature-, oxidation- and entropy-driven mixing) to synthesize and stabilize single-phase MEO nanoparticles containing up to ten cations, including a noble element. Compared with few-element nanoparticles, the denary oxide nanoparticles show superior structural stability, as proven by our simulations and in situ observations up to 1,073 K. Moreover, enabled by our rapid synthesis, we designed and screened a denary oxide nanoparticle catalyst with high activity and superior stability over 100 hours in the catalytic methane combustion reaction, demonstrating the promise of MEO nanoparticles as a material platform for highly stable catalyst discovery.

---

[1]Department of Materials Science and Engineering, University of Maryland, College Park, MD, USA. [2]Department of Mechanical and Industrial Engineering, University of Illinois at Chicago, Chicago, IL, USA. [3]Department of Chemical and Biomolecular Engineering, Johns Hopkins University, Baltimore, MD, USA. [4]Department of Mechanical Engineering and Materials Science, University of Pittsburgh, Pittsburgh, PA, USA. [5]Center for Nanophase Materials Sciences, Oak Ridge National Laboratory, Oak Ridge, TN, USA. [6]Department of Nano Engineering, Program of Materials Science and Engineering, University of California, San Diego, La Jolla, CA, USA. [7]Center for Materials Innovation, University of Maryland, College Park, MD, USA. [8]These authors contributed equally: Tangyuan Li, Yonggang Yao, Zhennan Huang, Pengfei Xie, Zhenyu Liu, Menghao Yang. ✉e-mail: guw8@pitt.edu; chaowang@jhu.edu; rsyassar@uic.edu; binghu@umd.edu

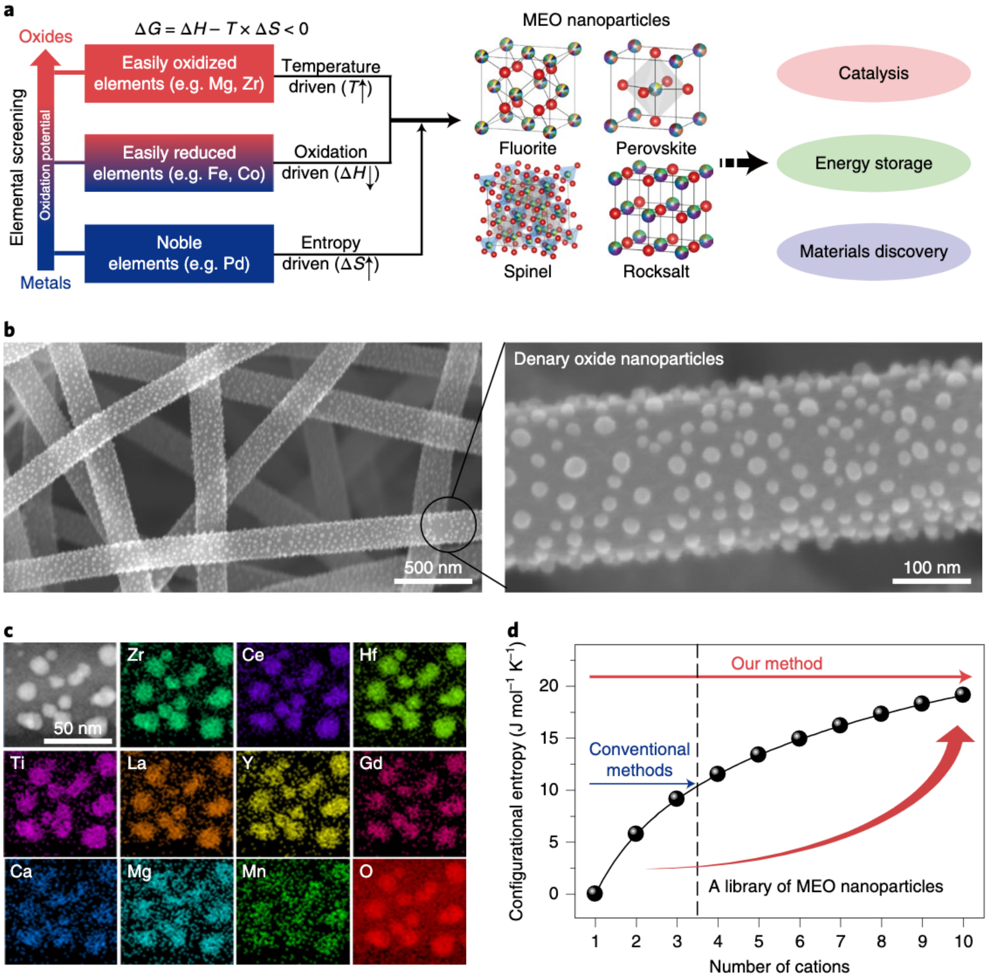

Fig. 1 | Compositional and structural design of MEO nanoparticles featuring up to ten cations. **a**, Synthesis of single-phase MEO nanoparticles based on three possible strategies (temperature-, oxidation- and entropy-driven mixing mechanisms) according to MEOs containing different elements. **b**, Low- and high-magnification SEM images, showing 10-MEO-MgMn nanoparticles uniformly dispersed on CNFs after synthesis. **c**, Elemental maps of 10-MEO-MgMn nanoparticles composed of ten cationic elements and oxygen (Zr, Ce, Hf, Ti, La, Y, Gd, Ca, Mg, Mn and O). **d**, Configurational entropy as a function of the number of cations. Our method enriches the compositional space of oxide nanoparticles featuring up to ten cations with a higher configurational entropy (calculation in the Methods).

Results

Rational design of MEO nanoparticles up to denary mixing. To accommodate the largely dissimilar elements in MEO nanoparticles, especially their different oxidation potentials, we have developed three rational design strategies for producing single-phase MEO nanoparticles with assorted structures (for example, fluorite, perovskite, rocksalt and spinel; Fig. 1a). These are temperature-driven mixing in MEOs containing easily oxidized elements; oxidation-driven mixing in MEOs containing easily reducible elements (by increasing the oxygen partial pressure during synthesis); and entropy-driven mixing by increasing the number of elements to enable the inclusion and stabilization of noble metals in MEOs. These strategies are based on the Gibbs free energy of the system ($\Delta G = \Delta H - T \times \Delta S$), in which increasing the synthesis temperature (T) and mixing entropy (ΔS), or decreasing the mixing enthalpy (ΔH) will help reduce the Gibbs free energy (ΔG) and hence favour the formation of single-phase MEOs.

To reveal the MEO formation process, we demonstrated the synthesis of denary oxide (Zr,Ce,Hf,Ti,La,Y,Gd,Ca,Mg,Mn)O_{2-x} nanoparticles (denoted as 10-MEO-MgMn, where x represents oxygen vacancy). First, we chose conductive carbon nanofibres (CNFs) as the substrate and utilized Joule heating to achieve rapid high-temperature heating with controllable magnitude and duration. In a typical process, multiple salt precursors of each element were mixed in the solution phase (0.05 mol l^{-1}) in equal molar amounts unless otherwise noted. The mixed precursor salt was uniformly coated onto the CNF substrate with a loading of 100 µl cm^{-2} (Extended Data Fig. 1a,b; see Methods for details). After high-temperature heating (for example, 1,500 K for 50 ms), scanning electron microscopy (SEM) imaging revealed the formation of homogeneous and high-density nanoparticles on the CNFs (Fig. 1b). In addition, we could easily tailor the particle size and distribution by tuning the duration of the synthesis: a shorter heating time leads to smaller particles with a narrower size distribution (Extended Data Fig. 1c).

Figure 1c shows scanning transmission electron microscopy (STEM) elemental maps of the 10-MEO-MgMn nanoparticles, which display homogeneous mixing of the 10 different elements throughout the nanoparticles without obvious elemental segregation or phase separation, thus indicating the successful synthesis of single-phase MEO nanoparticles. Note that the 10 cationic elements and their respective unary oxides have very different physiochemical properties, including a range of cation radii (0.74–1.16 Å) and crystal structures (for example, fluorite, rutile and rocksalt[25];

Supplementary Table 1), which would conventionally prevent single-phase homogeneous mixing. However, our ultrafast heating technique utilizes high temperatures to promote multi-element mixing for MEO nanoparticle formation while the heating duration is short enough to prevent particle coarsening and phase separation (Supplementary Fig. 1a). Accordingly, with this unique fast heating technique and the three MEO synthesis strategies, we have achieved a library of oxide nanoparticles with tunable compositions (from unary up to denary mixing) that are neither observed nor necessarily stable as bulk materials (Supplementary Fig. 1b and Supplementary Table 2). Compared with other synthetic methods, our strategy notably extends the compositional space, allowing us to enter the high-entropy regions of oxide nanoparticles (Fig. 1d).

Single-element screening and synthesis strategies of MEOs. Since oxide materials feature more complex element combinations than pure metals, the formation of single-phase MEO nanoparticles requires meticulous design and synthesis guidelines. The choice of elements is critical as some (for example, Ni, Cu and Pd) can be reduced to metals at high temperatures or by the reduction conditions (for example, carbon and 5%H_2/Ar)[26,27]. The oxide formation potential for an element has been well studied in metallurgy and evaluated by the Ellingham diagram,[24] which illustrates the formation Gibbs free energy of oxides at high temperature (Fig. 2a). Using the Ellingham diagram as a guide, we synthesized unary nanoparticles for 24 individual elements and identified which can form stable oxide nanoparticles using our high-temperature heating method (~1,500 K; Extended Data Fig. 2). After this single-element screening, the elements are divided into three categories (Fig. 2a): easily oxidized elements (shown in red; for example, Y, Ca, Ti and Zr); easily reducible elements (shown in blue, for example, Ni, Cu and Fe); and noble elements (for example, Pd), which provide a guideline for the compositional design and synthesis of MEO nanoparticles. Using temperature-, oxidation- and entropy-driven mixing strategies, we can accommodate these different ranges of oxidation potentials to successfully produce single-phase MEOs.

For MEOs containing easily oxidized elements, we use temperature-driven mixing. For example, phase separation was observed in the X-ray diffraction (XRD) pattern (Fig. 2b) of (Zr,Ce,Hf,Ti)O_x nanoparticles synthesized at ~1,000 K. However, by increasing the synthesis temperature to ~1,550 K, a single-phase fluorite structure was successfully achieved (Fig. 2b,e). Senary oxide (Zr,Ce,Hf,Ti,La,Y)O_{2-x} (fluorite, Extended Data Fig. 3a), denary oxide (Zr,Ce,Hf,Ti,La,Y,Gd,Ca,Mg,Mn)O_{2-x} (fluorite, Fig. 2c) and (Zr,Ce,Hf,Ti,La,Y,V,Nb,Ca,Mn)O_{2-x} (fluorite, Extended Data Fig. 3b), and quinary oxide (Ca,Mg)(Ti,Nb,Mn)O_{3-x} (perovskite) nanoparticles were also successfully synthesized in this manner, in which the XRD patterns (Fig. 2b), STEM atomic imaging (Fig. 2d) and TEM mapping (Fig. 2f) confirm single-phase structures.

For MEOs containing some easily reducible elements, we used oxidation-driven mixing by increasing the oxygen partial pressure (p_{O_2}) during the synthesis process, which allows further expansion of the MEO compositional space (Fig. 2g). For example, we were able to form homogeneous oxide (Fe,Co,Ni,Cu)O_x nanoparticles featuring a rocksalt structure from precursors containing Fe, Co, Ni and Cu by conducting the synthesis in air (a high p_{O_2}), as confirmed by the material's XRD, atomic structure and elemental mapping (Fig. 2h,i,k). By comparison, when a similar synthesis was done in an argon-filled glovebox (a low p_{O_2} of ~1 ppm), an fcc metal structure was observed (Fig. 2h). We also used this oxidation-driven strategy to synthesize oxide $(Mn,Fe,Co,Ni)_3O_{4-x}$ (spinel, Fig. 2h,j,l) and (Mg,Co,Ni,Zn,Cu)O nanoparticles (rocksalt, Extended Data Fig. 3c,d).

Finally, entropy-driven mixing in MEO nanoparticles can be used to include noble elements in the final product (for example, Pd, Fig. 2m). Temperature- and oxidation-driven mixing strategies are not enough to synthesize MEO nanoparticles with noble elements in their oxidation states. For example, we observed phase separation of the Pd metal and oxides in $(Zr,Ce,Hf)_{0.9}Pd_{0.1}O_x$ (Fig. 2n,o) synthesized at high temperature (~1,500 K) in air. However, by adding six more cations to the composition and effectively increasing the system's entropy, we were able to successfully synthesize 10-element MEO nanoparticles containing Pd (~10 at%) in its oxidized state (Fig. 2n,o), a composition that would otherwise lead to phase separation of metallic Pd if synthesized using conventional heating methods (Extended Data Fig. 4). The reasons for the inhibition of PdO decomposition to Pd in denary MEOs include entropy stabilization and the non-equilibrium synthesis. A similar result was also observed in the stabilization of oxidized Rh in denary MEOs (Supplementary Fig. 2). In addition, we also confirmed entropy-driven mixing in other MEOs containing easily reducible elements (for example Fe, Co) when synthesized in a low p_{O_2} (Extended Data Fig. 5).

Therefore, our unique fast heating/cooling process combined with temperature-, oxidation- and entropy-driven mechanisms provides effective strategies for the design and synthesis of MEO nanoparticles and significantly enriches the available library of oxide nanoparticles (MEO compositions and the related synthesis strategies are summarized in Supplementary Table 2).

Analysis of MEO formation and stability. To further validate the experimental results on single-phase MEO formation, we conducted density functional theory (DFT) calculations (Methods and Supplementary Methods) to analyse each thermodynamic parameter in the formation of a series of oxide systems (Fig. 3a–c and Supplementary Table 3). For example, the formation temperature of binary $(Zr,Ti)O_2$ from the corresponding unary oxide was predicted to be 2,828 K, whereas the quaternary $(Zr,Ce,Hf,Ti)O_2$ could form a single-phase structure at a temperature of just 1,075 K (Fig. 3a,b). This result indicates that a high temperature is necessary for single-phase MEO formation (temperature-driven mixing), whereas a lower formation temperature for a high entropy system with an increased number of components indicates the entropy-driven

Fig. 2 | Synthesis strategies for MEO nanoparticles. a, The formation Gibbs free energies of different oxides as a function of temperature (Ellingham diagram[24]), showing the oxidation potential of different elements. Easily oxidized elements are highlighted in red and blue shows easily reducible elements, as confirmed by our elemental screening. **b**, XRD patterns of (Zr,Ce,Hf,Ti)O_x synthesized at 1,000 K (phase separation), $(Zr,Ce,Hf,Ti)O_2$ (fluorite indexed to ZrO_2 (powder diffraction file (PDF) no. 49-1642)) at 1,550 K, and (Ca,Mg)(Ti,Nb,Mn)O_{3-x} (perovskite indexed to $CaTiO_3$ (PDF no. 22-0153)) nanoparticles at 1,550 K on CNFs. **c**,**d**, Atomic-resolution STEM images of 10-MEO-MgMn (fluorite; **c**) and (Ca,Mg)(Ti,Nb,Mn)O_{3-x} (perovskite; **d**) nanoparticles. **e**,**f**, Elemental maps of $(Zr,Ce,Hf,Ti)O_2$ (**e**) and (Ca,Mg)(Ti,Nb,Mn)O_{3-x} (**f**) nanoparticles showing uniform mixing of each element. Scale bar, 10 nm. **g**, Schematic of oxidation-driven mixing by increasing the p_{O_2} during synthesis. **h**, XRD patterns of (Fe,Co,Ni,Cu) by low p_{O_2} (~1 ppm) synthesis (metallic fcc structure), and (Fe,Co,Ni,Cu)O_x (rocksalt indexed to NiO (PDF no. 65-2901)) and $(Mn,Fe,Co,Ni)_3O_{4-x}$ (spinel indexed to Fe_3O_4 (PDF no. 65-3107)) nanoparticles by high p_{O_2} (air) synthesis. **i**,**j**, Elemental maps of (Fe,Co,Ni,Cu)O_x (**i**) and $(Mn,Fe,Co,Ni)_3O_{4-x}$ (**j**) nanoparticles. Scale bar, 10 nm. **k**,**l**, Atomic resolution STEM images of (Fe,Co,Ni,Cu)O_x (**k**) and $(Mn,Fe,Co,Ni)_3O_{4-x}$ (**l**) nanoparticles. **m**, Schematic of entropy-driven mixing in Pd-contained MEOs. **n**,**o**, XRD patterns (**n**) and elemental maps (**o**) of $(Zr,Ce,Hf)_{0.9}Pd_{0.1}O_x$ (phase-separation structure indexed to Pd (PDF no. 46-1043)) and (Zr,Ce,Hf,Ti,La,Y,Gd,Sm,Dy,Pd)O_{2-x} (fluorite) nanoparticles. Scale bar, 50 nm. $(Zr,Ce,Hf)_{0.9}Pd_{0.1}O_x$ showed a mixture of metallic Pd and oxides while Pd is stabilized at an oxidized state in denary oxide (Zr,Ce,Hf,Ti,La,Y,Gd,Sm,Dy,Pd)O_{2-x}.

mixing effect. We also found that the calculated Gibbs free energy of (Zr,Ce,Hf,Ti)O_2 decreases with increasing p_{O_2}, revealing the material's oxidation-driven stabilization (Fig. 3c). In addition, our DFT calculation results predict reasonable structural and chemical stability by considering lattice distortion and various decomposition pathways for the formed single-phase MEOs (Supplementary Figs. 3 and 4 and Supplementary Tables 4 and 5). Hence, the DFT results confirm that temperature, oxidation and entropy can play an important role in driving the formation of single-phase MEOs.

Although high temperatures are critical to overcome the kinetic barriers to multi-element mixing, we found that increasing temperature too far can adversely induce particle deterioration, such as

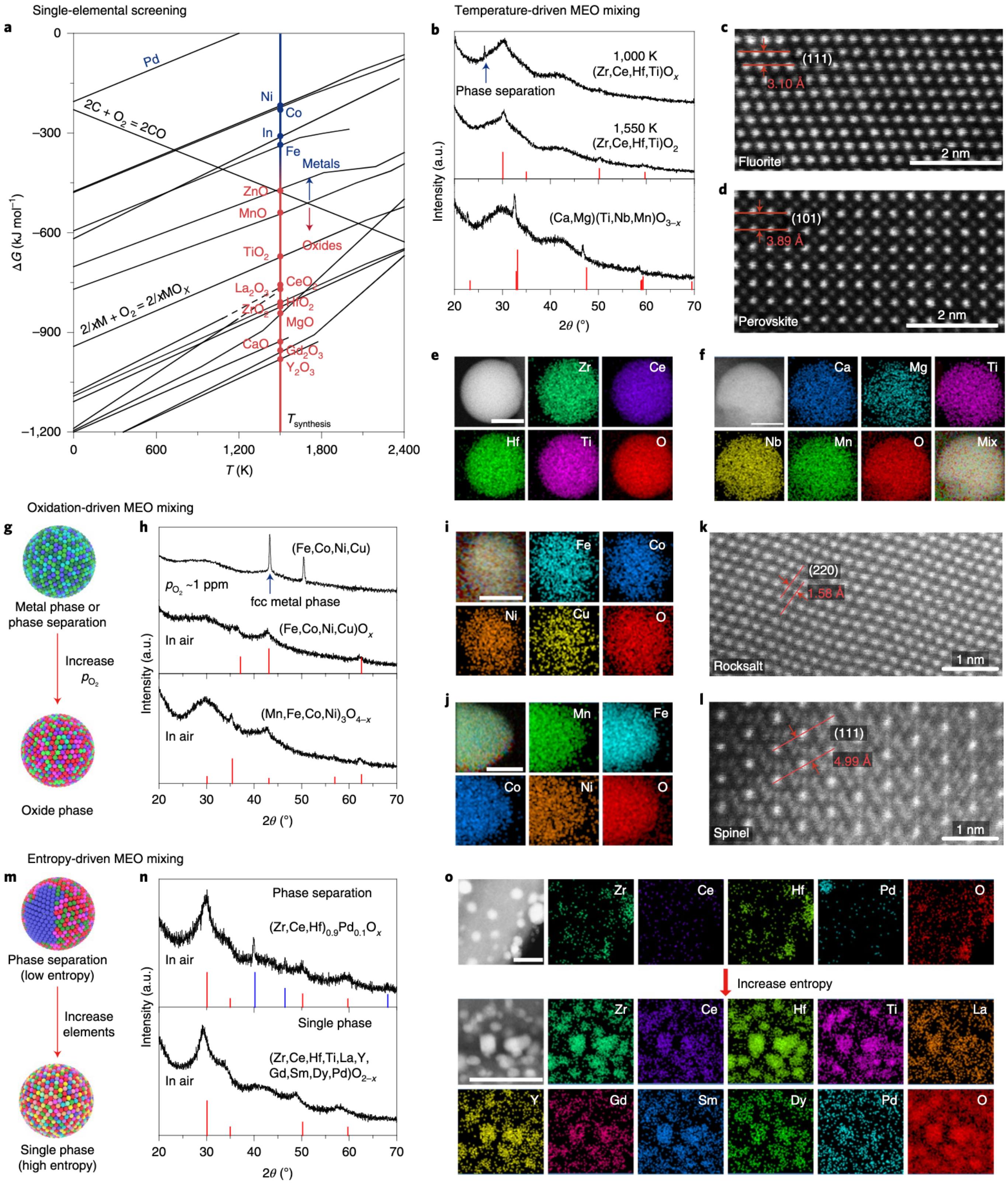

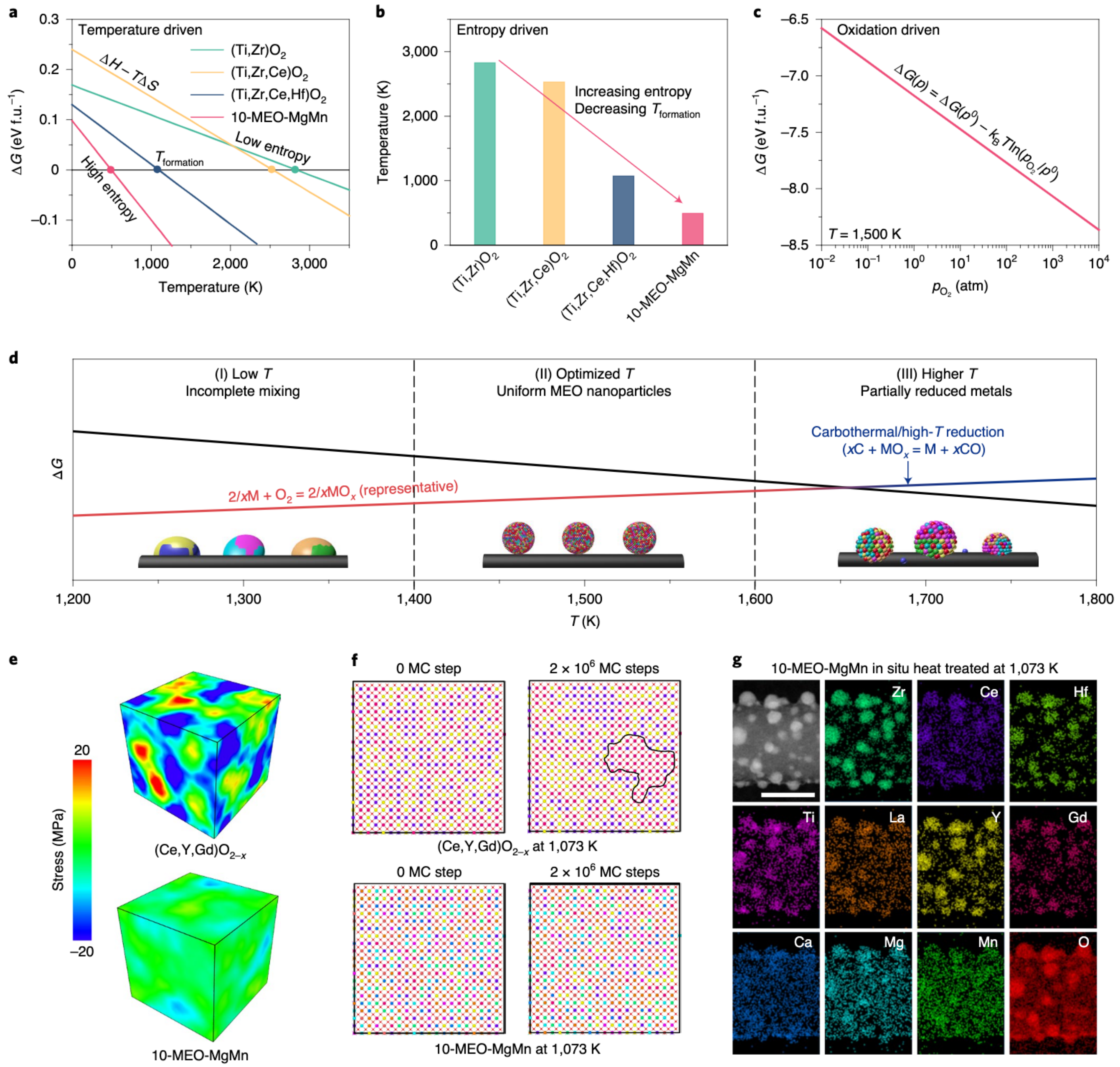

Fig. 3 | Thermodynamic analysis of MEO formation and their structural stability. a,**b**, Temperature-dependent formation Gibbs free energies (ΔG; **a**) and the magnitude of the formation temperature (**b**) of $(Ti,Zr)O_2$, $(Ti,Zr,Ce)O_2$, $(Ti,Zr,Ce,Hf)O_2$ and 10-MEO-MgMn derived from DFT calculations. A higher entropy leads to a lower formation temperature. The units (eV f.u.$^{-1}$) indicate electronvolts per formula unit. **c**, Variation of the predicted Gibbs free energy change for the formation of single-phase $(Ce,Zr,Hf,Ti)O_2$ as a function of the O_2 partial pressure. At a given temperature, the Gibbs free energy decreases with increasing p_{O_2}, indicating the MEO is more stable at high p_{O_2}. **d**, Schematic of the MEO nanoparticle synthesis at different synthetic temperatures associated with the Ellingham diagram: low temperature (~1,200 K; I) results in incomplete mixing due to the lack of energy; optimized temperature (~1,500 K; II) enables the formation of uniform MEO nanoparticles; and higher temperature (~1,800 K; III) causes particle overgrowth and carbon etching. **e**,**f**, The microscale stress distribution (**e**) and thermal stability (that is, after 2×10^6 Monte Carlo (MC) steps at 1,073 K) (**f**) for the ternary oxide $(Ce,Y,Gd)O_{2-x}$ and denary oxide 10-MEO-MgMn. The simulation results all indicate that the 10-MEO-MgMn is more thermodynamically and structurally stable than $(Ce,Y,Gd)O_{2-x}$, which features a lower mixing entropy. **g**, STEM elemental maps of the in situ heated 10-MEO-MgMn nanoparticles up to 1,073 K. Scale bar, 50 nm.

coarsening, aggregation and phase separation (for example, metallic impurities; Fig. 3d). For $(Zr,Ce,Hf,Ti,Mn,Co)O_{2-x}$ (Extended Data Fig. 6) at a low synthesis temperature of ~1,200 K, we did not experimentally observe formation of uniform nanoparticles on the CNFs, but rather terrace-shaped oxides because of the insufficient reaction. On the other hand, an increase of the synthesis temperature up to 1,800 K accelerates particle growth and aggregation (>80 nm), and introduces metal impurities (for example, Co) due to carbothermal reduction. Therefore, an optimized temperature (~1,500 K) is necessary to synthesize uniform MEO nanoparticles on CNFs to

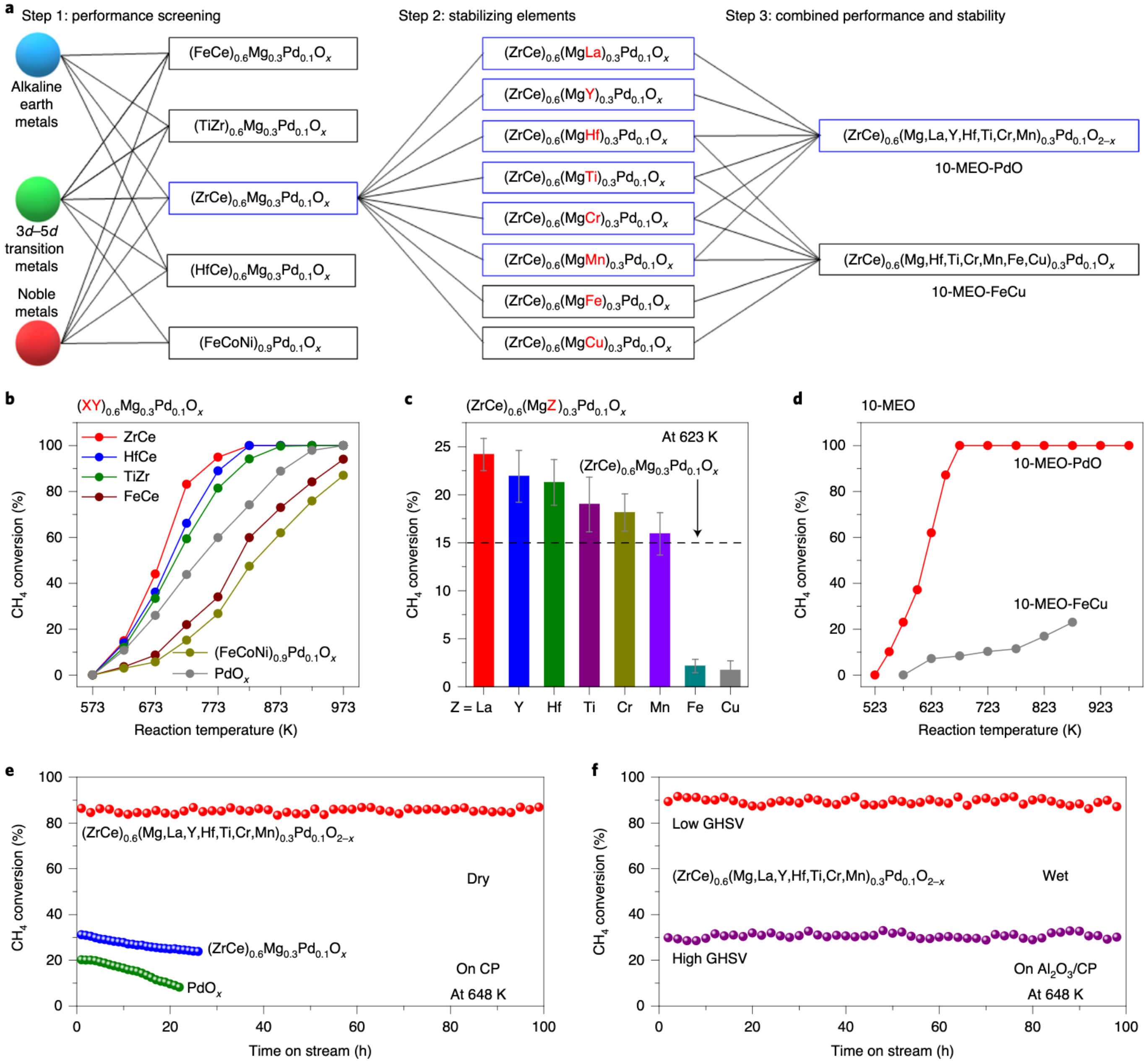

Fig. 4 | MEO catalyst design and screening for methane combustion. **a**, Schematic of the MEO catalyst design and three-step screening process. The designed MEO catalysts incorporate elements from different groups (alkaline earth, 3*d*–5*d* transition metal and Pd) for different functions (active sites, defects and so on). **b**, Temperature-dependent CH_4 conversion among multiple 4-MEOs. **c**, CH_4 conversion of a series of 5-MEOs with the composition of $(Zr,Ce)_{0.6}(Z)_{0.15}Mg_{0.15}Pd_{0.1}O_x$ at 623 K. The definition of the error bars can be found in the Methods. **d**, CH_4 conversion of $(Zr,Ce)_{0.6}(Mg,La,Y,Hf,Ti,Cr,Mn)_{0.3}Pd_{0.1}O_{2-x}$ (10-MEO-PdO) and other control sample of $(Zr,Ce)_{0.6}(Mg,Hf,Ti,Cr,Mn,Fe,Cu)_{0.3}Pd_{0.1}O_x$ (10-MEO-FeCu). Fe and Cu have a poisoning effect on the 10-MEO-FeCu sample. **e**, Catalytic stability of 10-MEO-PdO, $(Zr,Ce)_{0.6}Mg_{0.3}Pd_{0.1}O_x$ (4-MEO-Pd) and PdO_x on the carbon paper in terms of the samples' CH_4 conversion at 648 K under dry conditions using a GHSV of 10,800 $l\,g_{Pd}^{-1}\,h^{-1}$. **f**, Catalytic stability of 10-MEO-PdO on the Al_2O_3-coated carbon paper (CP) performed under wet conditions at 648 K using different GHSVs of 10,800 $l\,g_{Pd}^{-1}\,h^{-1}$ and 108,000 $l\,g_{Pd}^{-1}\,h^{-1}$.

provide just enough energy to mix all the elements and prevent the as-formed oxides from agglomerating and reacting with carbon.

Due to high-temperature synthesis and entropy stabilization, the MEO nanoparticles naturally possess excellent thermal stability. We performed molecular dynamic and Monte Carlo methods (Methods and Supplementary Methods) to simulate the structural and thermal stability of denary oxide $(Zr,Ce,Hf,Ti,La,Y,Gd,Ca,Mg,Mn)O_{2-x}$ (10-MEO-MgMn) and compared with ternary oxide $(Ce,Y,Gd)O_{2-x}$. Structurally, we modelled the average microscale stress density field in the simulated cell, and 10-MEO-MgMn shows a more uniform stress distribution than $(Ce,Y,Gd)O_{2-x}$, suggesting a relatively more stable structure (Fig. 3e). Furthermore, we simulated the structural evolutions during thermal annealing up to 1,073 K for these two MEO systems. This showed that the 10-MEO-MgMn persists as a homogeneous single-phase structure, whereas the $(Ce,Y,Gd)O_{2-x}$ is not stable and shows clear phase separation after thermal annealing at 1,073 K. Therefore, the denary 10-MEO-MgMn is more thermally stable than the ternary $(Ce,Y,Gd)O_{2-x}$ (Fig. 3f). To confirm this conclusion, we also simulated the structural stability of quaternary (Zr,Ce,Hf,Ti)O_2, which is slightly better than the ternary MEO but is comparably less stable than the denary MEO (Extended Data Fig. 7a,b).

Experimentally, we observed the structural stability of MEOs by heating ternary oxide (Ce,Gd,Y)O_{2-x}, quaternary oxide (Zr,Ce,Hf,Ti)O_2 and denary oxide 10-MEO-MgMn nanoparticles from 298 K up to 1,073 K by in situ STEM (the samples were stabilized at each temperature for 1 h before taking images). At 1,073 K, the 10-MEO-MgMn nanoparticles exhibit superior morphology and size stability, and maintain uniform mixing without phase separation (Fig. 3g). By contrast, changes in the morphology and size for the ternary sample, and elemental separation for both the ternary and quaternary oxides were observed (Extended Data Fig. 7c). These experimental results on the thermal stability of the MEOs are consistent with the force-field simulations and reveal the superior thermal stability of our denary MEO nanoparticles, which may be due to their high-entropy structure featuring both thermodynamic and kinetic stability. This confirmed excellent stability of our MEO nanoparticles is beneficial for practical applications.

Catalytic study of denary oxide nanoparticles. Our high-throughput synthesis method enables us to rationally design and rapidly explore a large library of MEO nanoparticles by mixing most elements in the periodic table. We now demonstrate how such MEO nanoparticles are particularly advantageous for catalytic applications and, more specifically, for methane combustion. The catalytic combustion of methane compared with traditional flame combustion is capable of stabilizing complete oxidation of fuel at low temperatures, while simultaneously reducing emissions (for example, NO_x)[28,29]. However, the PdO_x catalysts typically used for this reaction suffer from deactivation due to sintering of the nanoparticles and the transformation of PdO_x into metallic Pd during the reaction. Therefore, developing Pd-based catalysts with simultaneously enhanced performance and stability would effectively improve the energy efficiency of the catalytic CH_4 combustion process.

Figure 4a presents our strategy for designing and screening MEO catalysts for methane combustion, with steps as follows. When formulating the MEO catalysts, we included elements from different groups containing alkali metals, 3*d*–5*d* transition metals and the noble metal Pd, which provide distinct catalytic functions—promoting the transfer of electrons during the redox process, improving the redox capability and creating more oxygen defects, and activating CH_4, respectively[30,31]. The MEO catalysts were prepared using our high-temperature synthesis method with an oxide loading of ~2 wt% in each catalyst. Single-element PdO_x nanoparticles were also synthesized with similar Pd loadings and served as a control in this study.

In the first step we screened 4-MEO $(X,Y)_{0.6}Mg_{0.3}Pd_{0.1}O_x$ (where X and Y represent different metal elements) nanoparticles supported on carbon paper as catalysts for CH_4 combustion and compared with the PdO_x control sample. The catalytic activity was systematically measured at 573–973 K using a plug flow reactor with gas hourly space velocity (GHSV) = 10,800 $l\,g_{Pd}^{-1}\,h^{-1}$, with 5 vol% CH_4 and 20 vol% O_2 as the feeding gas, balanced by N_2. We confirmed that the bare carbon paper substrate did not degrade in air at temperatures below 973 K by thermal gravimetric analysis and additionally was inactive for CH_4 combustion (Supplementary Fig. 5). For all the 4-MEO catalysts, the reaction had an onset temperature of ~623 K and the CH_4 conversion increased with the reaction temperature (Fig. 4b). Among them, $(Zr,Ce)_{0.6}Mg_{0.3}Pd_{0.1}O_x$ shows the best performance (100% conversion at ~823 K), which is much more active than the control PdO_x (74% conversion at 823 K).

In the second step, after screening the 4-MEOs, eight different 3*d*–5*d* transition metals (Z = La, Y, Hf, Ti, Cr, Mn, Fe and Cu) were added to $(Zr,Ce)_{0.6}Mg_{0.3}Pd_{0.1}O_x$ to construct a series of 5-MEOs with the composition $(Zr,Ce)_{0.6}(Z)_{0.15}Mg_{0.15}Pd_{0.1}O_x$. The catalytic activities of the 5-MEO samples were measured at 623 K and compared with the 4-MEO $(Zr,Ce)_{0.6}Mg_{0.3}Pd_{0.1}O_x$ (dashed line in Fig. 4c, CH_4 conversion ~15%). When Z = La, Y, Hf, Ti, Cr or Mn, the 5-MEOs outperform $(Zr,Ce)_{0.6}Mg_{0.3}Pd_{0.1}O_x$ while a poison effect was observed with the addition of Fe and Cu.

Finally, by combining the six elements identified from the second screening step (La, Y, Hf, Ti, Cr and Mn) with the best-performing $(Zr,Ce)_{0.6}Mg_{0.3}Pd_{0.1}O_x$ (4-MEO-Pd), a denary oxide $(Zr,Ce)_{0.6}(Mg,La,Y,Hf,Ti,Cr,Mn)_{0.3}Pd_{0.1}O_{2-x}$ (10-MEO-PdO) was synthesized with the highest entropy among these MEO catalysts. The 10-MEO-PdO exhibited high catalytic activity compared with other catalysts (single PdO_x, 4-MEOs and 5-MEOs), reaching a complete conversion at 673 K (Fig. 4d). A control 9-MEO $(Zr,Ce)_{0.66}(Mg,La,Y,Hf,Ti,Cr,Mn)_{0.34}O_{2-x}$ sample (without Pd) was much less active for CH_4 combustion (Supplementary Fig. 6), indicating the importance of stabilizing Pd in the 10-MEO-PdO sample for improved catalytic performance. We have included detailed characterizations and simulated formation of 4-MEO-Pd and 10-MEO-PdO catalysts in Extended Data Fig. 8.

We also evaluated and compared the catalytic stability of PdO_x, the best-performing 4-MEO-Pd, and 10-MEO-PdO continuously at 648 K (after the catalytic reaction at 973 K, Fig. 4e). The high catalytic activity of the 10-MEO-PdO catalyst was extremely stable, with no discernible drop after 100 h, while the CH_4 conversion of the 4-MEO-Pd decreased from 31% to 20% after 26 h. By contrast, the CH_4 conversion of the PdO_x control dropped even faster, leading to deactivation after 22 h, which may be due to the reduction of PdO_x to metallic Pd during operation at high temperature[29,32], as we confirmed by XRD after the extended stability test (Extended Data Fig. 9a,b). The durability trend further confirms the advantages of the entropy effect ($(Zr,Ce)_{0.6}(Mg,La,Y,Hf,Ti,Cr,Mn)_{0.3}Pd_{0.1}O_{2-x} > (Zr,Ce)_{0.6}Mg_{0.3}Pd_{0.1}O_x > PdO_x$), which can stabilize Pd in a cationic state in the high-entropy structure for substantially improved overall catalyst stability. We also characterized the denary oxide 10-MEO-PdO catalyst after the 100 h durability test by elemental mapping (Extended Data Fig. 9c,d), observing nearly no change in the structural homogeneity.

To further stress the catalysts under harsh and practical applications, we evaluated the 10-MEO-PdO catalyst for methane combustion in the presence of water (~4 vol%). The carbon paper substrate was protected by a thin coating of Al_2O_3 (deposited using atomic layer deposition) to avoid accelerated carbon etching under wet conditions (Supplementary Fig. 7). The 10-MEO-PdO catalyst demonstrated a high activity of complete CH_4 conversion at ~673 K despite these harsh conditions (Extended Data Fig. 10). Figure 4f displays the catalytic stability of the denary sample under different GHSV values at 648 K. In particular, the higher GHSV of 108,000 $l\,g_{Pd}^{-1}\,h^{-1}$ ensures the stability evaluation was performed under the kinetically controlled regime. Notably, the 10-MEO-PdO sample showed stable performance in both cases for 100 h continuous operation, demonstrating the intrinsic stability of the catalyst. We also compared our sample with literature-reported catalysts[29,33–35], with which the 10-MEO-PdO shows similar performance and a superior stability (Supplementary Table 6). Therefore, our rapid synthesis method enables catalyst design and screening for a targeted reaction, and the high-entropy MEOs demonstrate great potential as high-performance and robust catalysts.

Conclusions

In summary, we have reported a method of designing highly stable denary oxide nanoparticle catalysts and other MEO nanoparticles with assorted structures. Three synthesis strategies (temperature-, oxidation- and entropy-driven multi-element mixing) were proposed to accommodate the dramatic differences (for example, oxidation potentials) among the multiple elements in these intrinsically complex systems. We also confirmed experimentally and computationally that denary MEOs with a larger compositional space demonstrate widely tailorable particle chemistry and superior thermal stability. Our work therefore opens a vast compositional space for oxide nanoparticles and enables high-throughput material synthesis and discovery for utilization in many technological fields.

Methods

Substrates and salt precursors. A solution of polyacrylonitrile with a concentration of 8 wt% in dimethylformamide was electrospun into polyacrylonitrile fibres at a voltage of 13 kV and a spinning distance of 15 cm. These as-spun films were first stabilized at 553 K for 6 h in air and then carbonized at 1,273 K for 2 h in argon to prepare the CNFs used in our experiments. Carbon paper (AvCarb MGL190) used in the test of thermal catalysis was purchased from Fuel Cell Store. The Al_2O_3 coating was grown on the surface of carbon paper using atomic layer deposition (Beneq TFS 500). All chemicals were purchased from Sigma Aldrich. Salts, including $CeN_3O_9{\cdot}6H_2O$ (99.0%), $LaN_3O_9{\cdot}6H_2O$ (99.99%), $YN_3O_9{\cdot}6H_2O$ (99.9%), $CaN_2O_6{\cdot}4H_2O$ (99.0%), $MgN_2O_6{\cdot}6H_2O$ (99.0%), $GdN_3O_9{\cdot}6H_2O$ (99.9%), $MnN_2O_6{\cdot}4H_2O$ (97.0%), $FeN_3O_9{\cdot}9H_2O$ (98.0%), $CoN_2O_6{\cdot}6H_2O$ (98.0%), $CuN_2O_6{\cdot}6H_2O$ (98.0%), $NiN_2O_6{\cdot}6H_2O$ (98.0%), $InN_3O_9{\cdot}xH_2O$ (99.9%), $CrN_3O_9{\cdot}9H_2O$ (99.0%), $ZnN_2O_6{\cdot}6H_2O$ (98.0%), $PdCl_2$ (99.0%), $HfCl_4$ (99.9%), $ZrCl_4$ (99.9%), $TiCl_4$ (99.9%), VCl_3 (97.0%) and $NbCl_5$ (99.9%) were dissolved in ethanol:water mixtures with a volume ratio of 9:1 to prepare the different salt solutions ($0.05\,\mathrm{mol\,l^{-1}}$). Different salts were chosen and mixed at equimolar amounts in the multi-element synthesis. These solutions were loaded onto the CNF films with a loading of $100\,\mathrm{\mu l\,cm^{-2}}$ and then dried at room temperature prior to high-temperature heating.

High-temperature heating. High-temperature synthesis by electrical Joule heating was carried out in an argon atmosphere (p_{O_2}: ~1 ppm) or controlled oxygen partial pressure (high p_{O_2}: in air). The CNF or carbon paper film were cut to sizes of 5 mm × 20 mm, which were adhered to copper electrodes supported by glass slides using silver paste and then connected with a current supply (HY6020EX-60A, VOL TEQ, and Keithley 2425, Tektronix). Different input currents were applied to the material and the resulting high temperature emitted light, which was recorded using a high-speed camera (Vision Research Phantom v.12.0) to determine the sample temperature[36].

Material characterization. XRD spectra of the substrates decorated with nanoparticles were collected using a diffractometer (D8 Advance, Bruker) with Cu Kα radiation at room temperature. Raman measurements were carried out on a Horiba Jobin-Yvon spectrometer using a 532 nm laser and an integration time of 4 s. Sample morphologies were revealed by field emission SEM (SU-70, Hitachi). The microstructures of the samples were observed using transmission electron microscopy (TEM; JEM-2100, JEOL) and STEM (JEM-ARM200F, JEOL) operated at 200 kV. Elemental maps were obtained using energy dispersive spectroscopy (EDS; X-Max^N-100TLE, Oxford Instruments). In situ STEM heating was performed at 298 K, 773 K and 1,073 K, and the sample was kept at each temperature for 1 h before collecting the EDS data and image. The particle size and distribution were determined using ImageJ software. X-ray photoelectron spectroscopy results were determined with an AXIS 165 spectrometer (Kratos).

Calculation of the configurational entropy. The configurational entropy ($\Delta S_{\mathrm{config}}$) increases with the number of cations, which can be calculated for our MEO materials (for example, fluorite oxides (MO_2), in which M is the cationic element) using the formula:

$$\Delta S_{\mathrm{config}} = -R \times \left(\sum_{i=1}^{n} x_i \ln x_i \right)_{\mathrm{M\text{-}site}} \tag{1}$$

in which R is the gas constant, x_i represents the mole fractions of the metal cations, M-site refers to the cationic site, and n is the total number of cations. In the calculation, equiatomic cations were considered and the existence of possible oxygen defects was ignored based on an ideal mixture.

Modelling of the thermodynamic stability of MEOs. Spin-polarized DFT calculations were performed using the Vienna Ab-initio Simulation Package (VASP), with plane wave basis and projector-augmented wave (PAW) formulism[37,38]. Exchange-correlation energy functionals, as determined by Perdew–Burke–Ernzerhof under the generalized-gradient approximation (GGA), were employed[39]. A kinetic energy cutoff of 500 eV was used for plane wave expansion. For the electronic relaxation, the total energy was converged to 10^{-6} eV. For the ionic relaxation, the structures were optimized until the force acting on each atom was below $0.01\,\mathrm{eV\,Å^{-1}}$. The equilibrium lattice parameters were determined by fitting the total energy to the Birch–Murnaghan equation of state[40]. In this work, we used DFT to analyse each thermodynamic parameter in the formation of a series of MEOs, as well as the lattice distortion and decomposition pathways of the materials. Detailed discussions and the optimized MEO structures can be found in the Supplementary Methods and Supplementary Data 1.

Large-scale simulation of MEOs. Large-scale atomic simulations were performed for MEOs with dimensions of $54.7 \times 54.7 \times 54.7\,\mathrm{Å^3}$ containing 12,000 atoms. We developed random and genetic algorithm sampling statistical methods to generate the representative configurations for the ternary, quaternary and denary oxides. Starting from the representative configurations of the MEOs, we analysed their structural stability by evaluating their stress distribution in Molecular Dynamic simulations, as well as their thermal stability by the thermal annealing process in Monte Carlo simulations. In addition, we calculated the thermodynamic formation of the MEOs. Detailed discussions and initial and final configurations of the MEOs can be found in the Supplementary Methods and Supplementary Data 2.

Measurement of catalytic performance. Catalytic methane combustion was conducted in a fixed-bed flow reactor at atmospheric pressure. Denary oxide nanoparticles were formed on the carbon paper or Al_2O_3-coated carbon paper with a loading of ~2 wt% using our high-temperature strategy. The carbon paper used was first activated at 1,173 K for 180 min in a carbon dioxide atmosphere. We have confirmed that the carbon paper and Al_2O_3-coated carbon paper are stable up to 973 K (Extended Data Fig. 10b). For the control PdO_x sample, we used an impregnation method (that is, the precursors were first loaded onto the carbon paper and then the sample was thermally treated ($3\,\mathrm{K\,min^{-1}}$, 773 K, 120 min) in a furnace with air atmosphere) to prepare particles with the same Pd loading. The catalyst (50 mg; carbon paper with oxide loading of 2 wt%) was loaded into a microflow quartz reactor (7 mm inner diameter). The catalyst bed was placed between quartz wool plugs in the reactor. The catalyst was heated to 473 K, 523 K or 573 K at a rate of $5\,\mathrm{K\,min^{-1}}$ under N_2 ($20\,\mathrm{ml\,min^{-1}}$), and the gas flow was then switched to the reactant feeds ($18\,\mathrm{ml\,min^{-1}}$, space velocity = $10{,}800\,\mathrm{l\,g_{Pd}^{-1}\,h^{-1}}$ or $180\,\mathrm{ml\,min^{-1}}$, space velocity = $108{,}000\,\mathrm{l\,g_{Pd}^{-1}\,h^{-1}}$). The reactants, CH_4 (99.99%) and O_2 (99.999%), with N_2 as the balance, were co-fed into the reactor using calibrated mass flow controllers with a CH_4:O_2 molar ratio of 1:4. For testing the catalytic performance in the presence of water, ~4 vol% H_2O was added to the gas feed using a steam generator maintained at 303 K. The reaction temperature was increased stepwise from 473 K, 523 K or 573 K to 973 K, and the reaction was carried out at each temperature until the conversion became constant. Error bars were obtained by standard deviation calculations for three trials. To determine the conversions of the reactants and the formation of products, a gas chromatograph (GC-2010 plus, Shimadzu) was employed, equipped with a silica capillary column (SH-Rt-Q-BOND) and a barrier ionization discharge detector. All of the lines between the reactor outlet and GC sampling loop inlet were heat-traced to 423 K to prevent product condensation. Methane conversion was calculated as follows:

$$\mathrm{CH_4\ conversion\ (\%)} = \frac{[\mathrm{CH_4}]_{\mathrm{inlet}} - [\mathrm{CH_4}]_{\mathrm{outlet}}}{[\mathrm{CH_4}]_{\mathrm{inlet}}} \times 100 \tag{2}$$

Data availability

Experimental procedures and material characterization of the oxide nanoparticles are available within this paper and the Methods. Powder diffraction file (PDF) cards of compounds used in this work are available at the Joint Committee on Powder Diffraction Standards. The atomic coordinates of the optimized oxide structure and initial and final configurations of the oxides are provided in the Supplementary Data. Other data that support the plots within this paper and the findings of this study are available from the corresponding authors on reasonable request.

Code availability

Density functional theory calculations on the formation of multi-element oxides were performed using VASP. The structural and thermal stabilities of multi-element oxides were computed by applying the Large-scale Atomic/Molecular Massively Parallel Simulator (LAMMPS). The open-source LAMMPS computer code is available at https://lammps.sandia.gov. The parameters used for the calculations are listed in the Methods, Supplementary Methods or available from the corresponding author upon reasonable request.

Received: 8 March 2020; Accepted: 18 November 2020;
Published online: 11 January 2021

References

1. Liao, L. et al. Efficient solar water-splitting using a nanocrystalline CoO photocatalyst. *Nat. Nanotechnol.* **9**, 69–73 (2013).
2. Bergmann, A. et al. Unified structural motifs of the catalytically active state of Co(oxyhydr)oxides during the electrochemical oxygen evolution reaction. *Nat. Catal.* **1**, 711–719 (2018).
3. Li, M., Schnablegger, H. & Mann, S. Coupled synthesis and self-assembly of nanoparticles to give structures with controlled organization. *Nature* **402**, 393–395 (1999).

4. Feng, X. et al. Converting ceria polyhedral nanoparticles into single-crystal nanospheres. *Science* **312**, 1504–1508 (2006).
5. Feng, K. et al. Cu$_x$Co$_{1-x}$O nanoparticles on graphene oxide as a synergistic catalyst for high-efficiency hydrolysis of ammonia-borane. *Angew. Chem. Int. Ed.* **55**, 11950–11954 (2016).
6. Rost, C. M. et al. Entropy-stabilized oxides. *Nat. Commun.* **6**, 8485 (2015).
7. Gild, J., Samiee, M., Braun, L., Harrington, T. & Vega, H. High-entropy fluorite oxides. *J. Eur. Ceram. Soc.* **38**, 3578–3584 (2018).
8. Oses, C., Toher, C. & Curtarolo, S. High-entropy ceramics. *Nat. Rev. Mater.* **5**, 295–309 (2020).
9. Dai, S. Across the board: Sheng Dai on catalyst design by entropic factors. *ChemSusChem* **13**, 1915–1917 (2020).
10. Sarkar, A. et al. High entropy oxides for reversible energy storage. *Nat. Commun.* **9**, 3400 (2018).
11. Chen, H. et al. Entropy-stabilized metal oxide solid solutions as CO oxidation catalysts with high-temperature stability. *J. Mater. Chem. A* **6**, 11129–11133 (2018).
12. Chen, H. et al. Mechanochemical synthesis of high entropy oxide materials under ambient conditions: dispersion of catalysts via entropy maximization. *ACS Mater. Lett.* **1**, 83–88 (2019).
13. Sun, S. & Zeng, H. Size-controlled synthesis of magnetite nanoparticles. *J. Am. Chem. Soc.* **124**, 8204–8205 (2002).
14. Pang, X., Zhao, L., Han, W., Xin, X. & Lin, Z. A general and robust strategy for the synthesis of nearly monodisperse colloidal nanocrystals. *Nat. Nanotechnol.* **8**, 426–431 (2013).
15. Du, J. S. et al. The structural fate of individual multicomponent metal-oxide nanoparticles in polymer nanoreactors. *Angew. Chem. Int. Ed.* **56**, 7625–7629 (2017).
16. Anandkumar, M., Bhattacharya, S. & Deshpande, A. S. Low temperature synthesis and characterization of single phase multi-component fluorite oxide nanoparticle sols. *RSC Adv.* **9**, 26825–26830 (2019).
17. Rajeeva, B. B. et al. Accumulation-driven unified spatiotemporal synthesis and structuring of immiscible metallic nanoalloys. *Matter* **1**, 1606–1617 (2019).
18. Patzke, G. R., Zhou, Y., Kontic, R. & Conrad, F. Oxide nanomaterials: synthetic developments, mechanistic studies, and technological innovations. *Angew. Chem. Int. Ed.* **50**, 826–859 (2011).
19. Haber, J. A., Anzenburg, E., Yano, J., Kisielowski, C. & Gregoire, J. M. Multiphase nanostructure of a quinary metal oxide electrocatalyst reveals a new direction for OER electrocatalyst design. *Adv. Energy Mater.* **5**, 1–11 (2015).
20. Cheng, F. et al. Rapid room-temperature synthesis of nanocrystalline spinels as oxygen reduction and evolution electrocatalysts. *Nat. Chem.* **3**, 79–84 (2011).
21. Li, S., Ren, Y., Biswas, P. & Tse, S. D. Flame aerosol synthesis of nanostructured materials and functional devices: processing, modeling, and diagnostics. *Prog. Energy Combust. Sci.* **55**, 1–59 (2016).
22. Mialon, G., Gohin, M., Gacoin, T. & Boilot, J. High temperature strategy for oxide nanoparticle synthesis. *ACS Nano* **2**, 2505–2512 (2008).
23. Lu, Z. et al. Identifying the active surfaces of electrochemically tuned LiCoO$_2$ for oxygen evolution reaction. *J. Am. Chem. Soc.* **139**, 6270–6276 (2017).
24. Reed, T. B. *Free Energy of Formation of Binary Compounds* (MIT Press, 1971).
25. Shannon, R. D. Revised effective ionic radii and systematic studies of interatomie distances in halides and chaleogenides. *Acta Cryst.* **32**, 751–767 (1976).
26. Yao, Y. et al. Carbothermal shock synthesis of high-entropy-alloy nanoparticles. *Science* **359**, 1489–1494 (2018).
27. Neagu, D., Tsekouras, G., Miller, D. N., Ménard, H. & Irvine, J. T. S. In situ growth of nanoparticles through control of non-stoichiometry. *Nat. Chem.* **5**, 916–923 (2013).
28. J Farrauto, R. Low-temperature oxidation of methane. *Science* **337**, 659–661 (2012).
29. Al, F. et al. Exceptional activity for methane combustion over modular Pd@CeO$_2$. *Science* **337**, 713–718 (2012).
30. Zarur, A. J. & Ying, J. Y. Reverse microemulsion synthesis of nanostructured complex oxides for catalytic combustion. *Nature* **403**, 65–67 (2000).
31. Li, W. B., Wang, J. X. & Gong, H. Catalytic combustion of VOCs on non-noble metal catalysts. *Catal. Today* **148**, 81–87 (2009).
32. Peng, H. et al. Confined ultrathin Pd-Ce nanowires with outstanding moisture and SO$_2$ tolerance in methane combustion. *Angew. Chem.* **130**, 9091–9095 (2018).
33. Nguyen, T. S. et al. Correlation of the ratio of metallic to oxide species with activity of PdPt catalysts for methane oxidation. *Catal. Sci. Technol.* **10**, 1408–1421 (2020).
34. Toso, A., Colussi, S., Padigapaty, S., de Leitenburg, C. & Trovarelli, A. High stability and activity of solution combustion synthesized Pd-based catalysts for methane combustion in presence of water. *Appl. Catal. B* **230**, 237–245 (2018).
35. Willis, J. J. et al. Systematic identification of promoters for methane oxidation catalysts using size- and composition-controlled Pd-based bimetallic nanocrystals. *J. Am. Chem. Soc.* **139**, 11989–11997 (2017).
36. Jacob, R. J. et al. High speed 2-dimensional temperature measurements of nanothermite composites: probing thermal vs. gas generation effects. *J. Appl. Phys.* **123**, 115902 (2018).
37. Kresse, G. & Furthmüller, J. Efficient iterative schemes for ab initio total-energy calculations using a plane-wave basis set. *Phys. Rev. B* **54**, 11169–11186 (1996).
38. Kresse, G. & Joubert, D. From ultrasoft pseudopotentials to the projector augmented-wave method. *Phys. Rev. B* **59**, 3–4 (1999).
39. Perdew, J. P., Burke, K. & Ernzerhof, M. Generalized gradient approximation made simple. *Phys. Rev. Lett.* **77**, 3865–3868 (1996).
40. Birch, F. Finite elastic strain of cubic crystals. *Phys. Rev.* **71**, 809–824 (1947).

Acknowledgements

This project is not directly funded. We thank D. J. Kline and M. R. Zachariah for their assistance with temperature measurements. R.S.-Y. and Z.H., and electron microscopy studies were supported by NSF-DMR award no.1809439. Z.L. and G.W. acknowledge computational resources provided by the University of Pittsburgh Center for Research Computing as well as the Extreme Science and Engineering Discovery Environment (XSEDE), which is supported by National Science Foundation grant no. ACI-1053575. M.C. acknowledges the Center for Nanophase Materials Sciences, which is a US Department of Energy Office of Science User Facility.

Author contributions

L.H., T.L. and Y.Y. contributed to the idea and experimental design. T.L., Y.Y., J.G., A.H.B., G.P., M.J., Q.D., J.D. and S.L. conducted materials preparation and characterization. Z.H., M.C. and R.S.-Y. carried out the high-resolution microscopy. P.X., K.Z., H.Z. and C.W. performed the catalysis measurements. J.L. contributed to experimental analysis. Z.L. and G.W. conducted the DFT simulations. M.Y. and Y.M. conducted the MD simulations. L.H., T.L. and Y.Y. wrote the paper, and all authors commented on the final manuscript.

Competing interests

The authors declare no competing interests.

Additional information

Extended data is available for this paper at https://doi.org/10.1038/s41929-020-00554-1.

Supplementary information is available for this paper at https://doi.org/10.1038/s41929-020-00554-1.

Correspondence and requests for materials should be addressed to L.H., R.S.-Y., C.W. or G.W.

Peer review information *Nature Catalysis* thanks Wangcheng Zhan and the other, anonymous, reviewer(s) for their contribution to the peer review of this work.

Reprints and permissions information is available at www.nature.com/reprints.

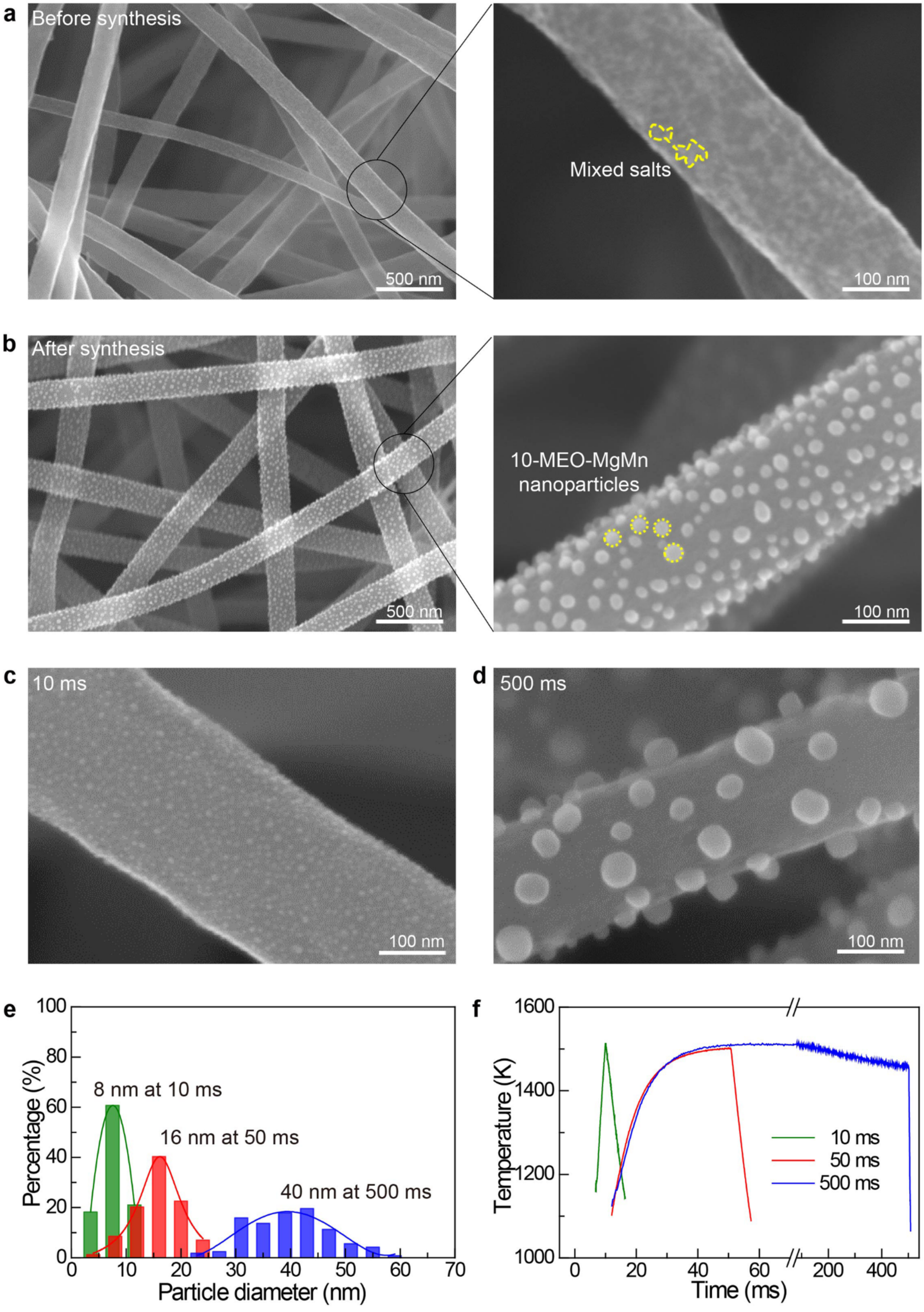

Extended Data Fig. 1 | See next page for caption.

Extended Data Fig. 1 | 10-MEO-MgMn sample before and after the high-temperature synthesis and size control. **a**, SEM images of the sample prior to synthesis. Mixed salt precursors were uniformly loaded onto the CNF substrate. **b**, SEM images of the 10-MEO-MgMn nanoparticles uniformly dispersed on the CNFs by the high-temperature conditions (1500 K, 50 ms). **c**, **d**, SEM images of the 10-MEO-MgMn nanoparticles synthesized at different durations, including 10 ms (**c**) and 500 ms (**d**) at 1500 K. **e**, Particle size distribution of the 10-MEO-MgMn nanoparticles made at 1500 K and at different durations. **f**, Temperature profiles used in our synthesis. High temperature (~1500 K), short time (within 1 second), and high cooling rate (~10^4 K/s) are beneficial for the MEO nanoparticle formation.

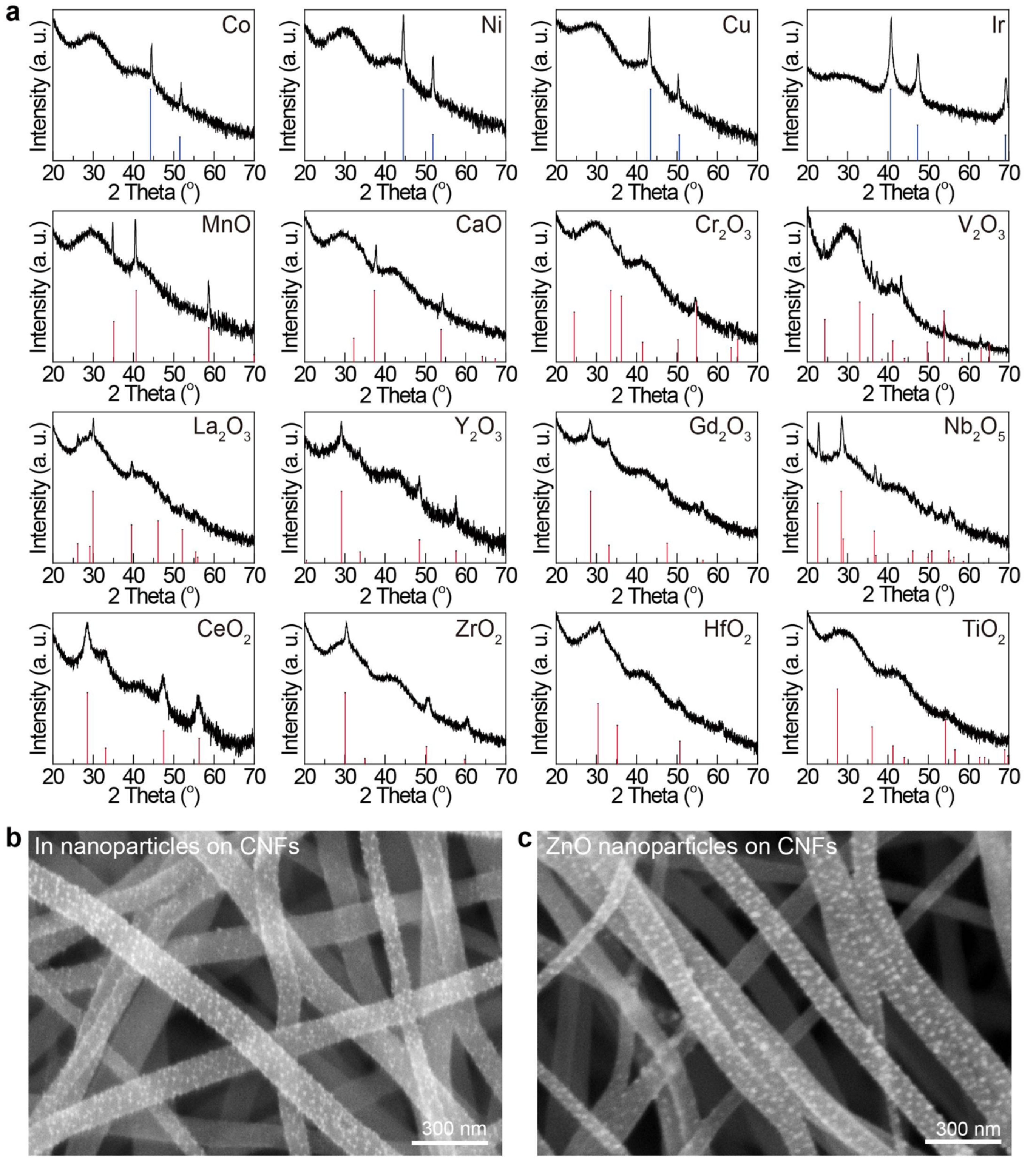

Extended Data Fig. 2 | XRD and SEM patterns of unary metal and oxide nanoparticles dispersed on the CNF substrate. a, XRD patterns. The formation of unary metal (for example, Co, Ni) and oxide (for example, MnO, CaO) nanoparticles is closely related to the Ellingham diagram (Fig. 2a in the main text). Elements above the carbothermic reduction curve ($2C+O_2=2CO\uparrow$) are easily reduced to metallic states, while those elements beneath the curve can maintain their oxidized states after the high-temperature synthesis (~1500 K). **b**, **c**, SEM images of metal In (**b**) and oxide ZnO (**c**) nanoparticles on CNFs. The SEM images and their XRD patterns demonstrate the formation of unary metal or oxide nanoparticles using our high-temperature synthesis.

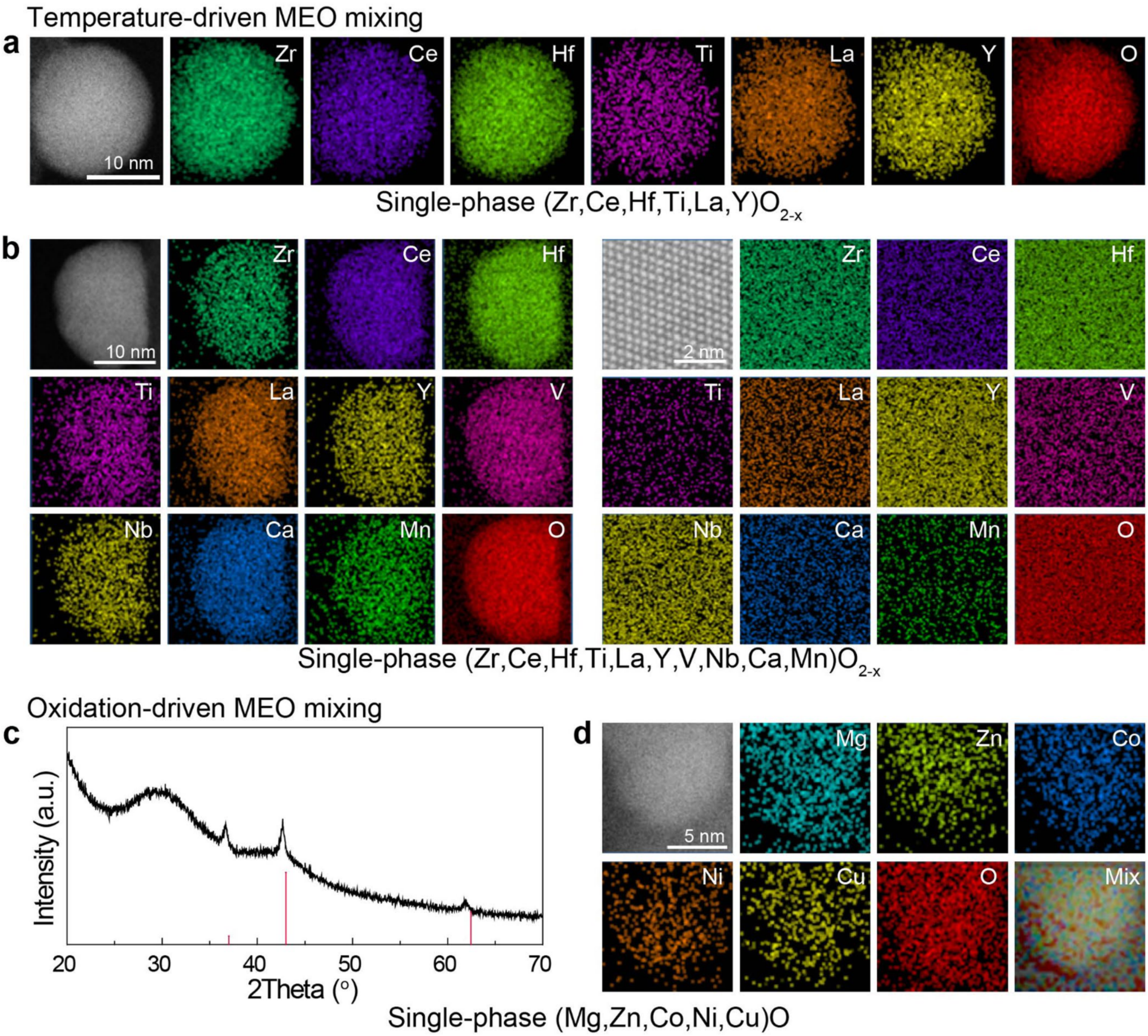

Extended Data Fig. 3 | MEO nanoparticles synthesized by temperature- and oxidation-driven strategies. a, **b**, Elemental mapping of single-phase (Zr,Ce,Hf,Ti,La,Y)O$_{2-x}$ (**a**) and denary (Zr,Ce,Hf,Ti,La,Y,V,Nb,Ca,Mn)O$_{2-x}$ (**b**) nanoparticles by temperature-driven mixing. **c**, **d**, XRD (**c**) and elemental mapping (**d**) of (Mg,Zn,Co,Ni,Cu)O nanoparticles synthesized by oxidation-driven mixing, showing a single-phase rocksalt (indexed to MgO (PDF#65-0476)) structure.

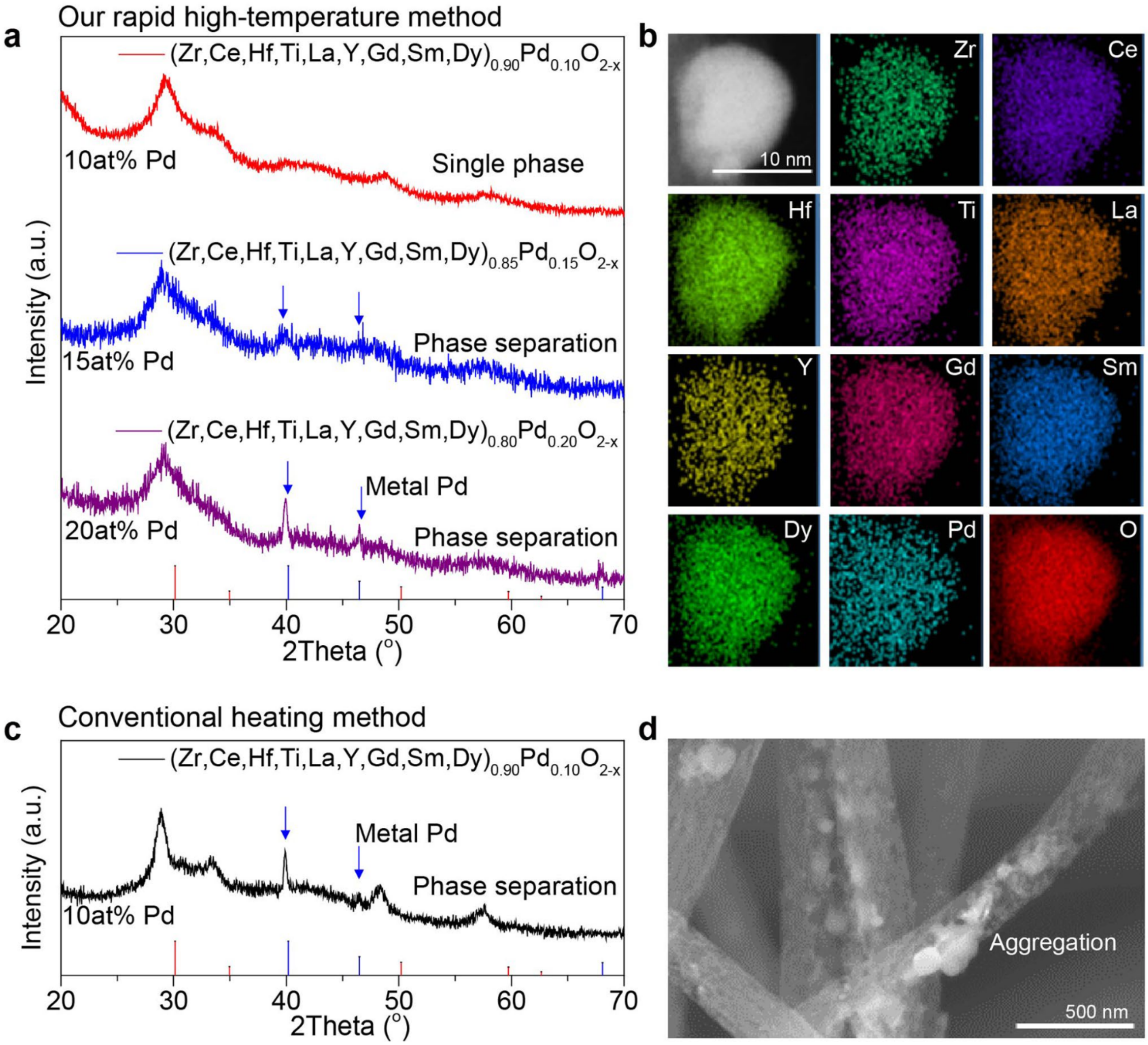

Extended Data Fig. 4 | The stabilization of Pd in the denary oxide nanoparticles. **a**, XRD patterns of samples synthesized by our rapid high-temperature synthesis, including denary MEOs with noble Pd content of 10at% (single phase), 15at% (phase separation), and 20at% (phase separation). In these samples with higher Pd contents, although the strategy of entropy-driven mixing and rapid synthesis was used, the metallic Pd phase starts to emerge due to increasing concentration of Pd in MEOs, which lowers the diffusion distance and eventually causes phase separation and reduction of Pd. **b**, Elemental mapping of the denary MEO with 10at% Pd, showing uniform elemental mixing. **c**, XRD and **d**, SEM of the denary MEO with 10at% Pd synthesized by the conventional heating method (annealed under Ar at 1,273 K for 2 h), showing phase separation and particle aggregation. This result suggests the capability of our high-temperature non-equilibrium method to synthesize and stabilize the noble element into single-phase MEO nanoparticles.

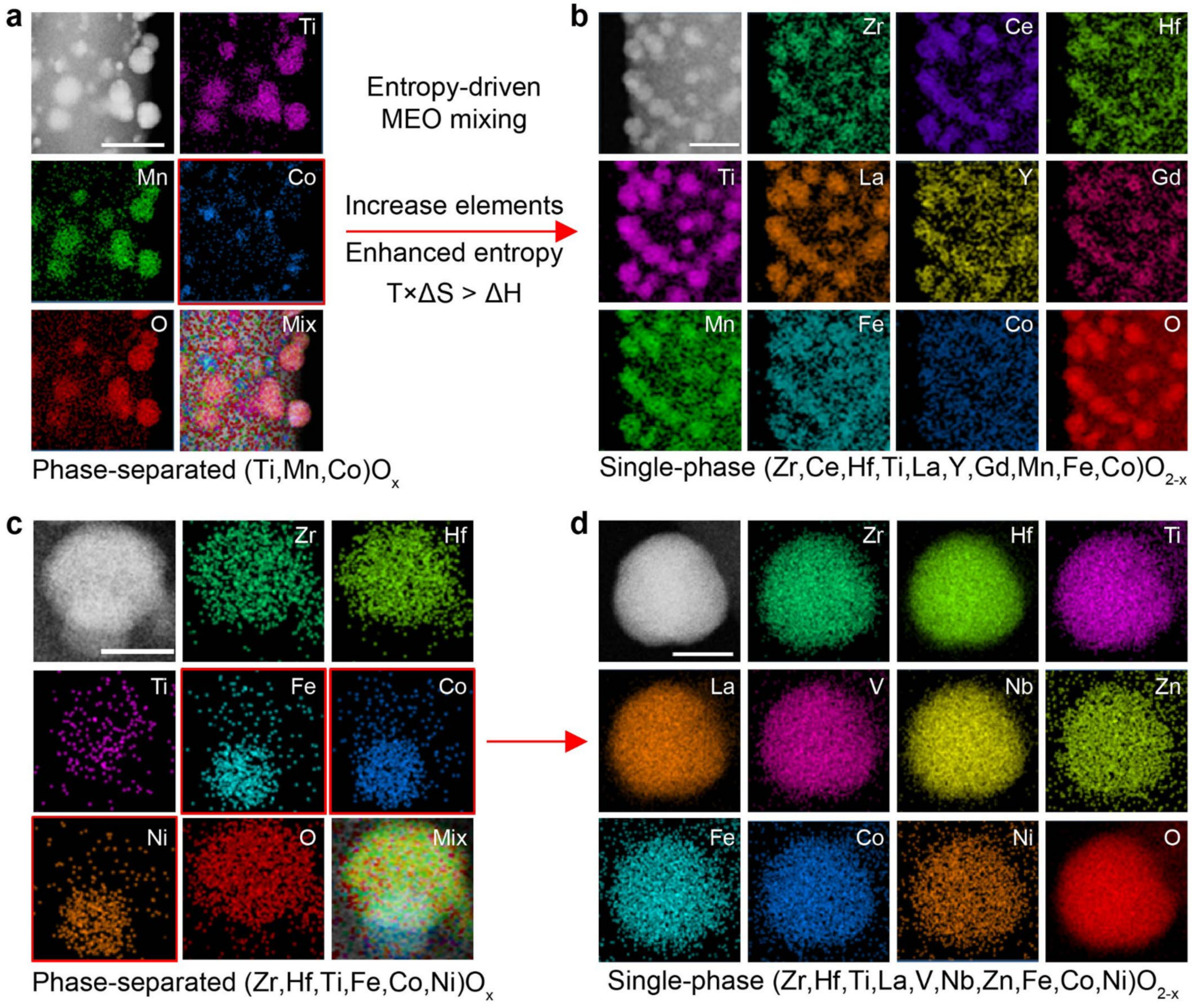

Extended Data Fig. 5 | MEO nanoparticles synthesized by entropy-driven strategies. a, **b**, Elemental mapping of ternary oxide (Ti,Mn,Co)O_x (**a**) showing phase separation of Co from other elements. By adding 7 more elements, the denary oxide (Zr,Ce,Hf,Ti,La,Y,Gd,Mn,Fe,Co)O_{2-x} (**b**) shows single-phase MEO formation, indicating entropy-driven mixing effect. Scale bar = 50 nm. **c**, **d**, Elemental mapping of senary oxide (Zr,Hf,Ti,Fe,Co,Ni)O_x (phase separation) (**c**) and denary oxide (Zr,Hf,Ti,La,V,Nb,Zn,Fe,Co,Ni)O_{2-x} (single phase) (**d**) nanoparticles, showing the similar entropy-driven effect. Scale bar = 10 nm.

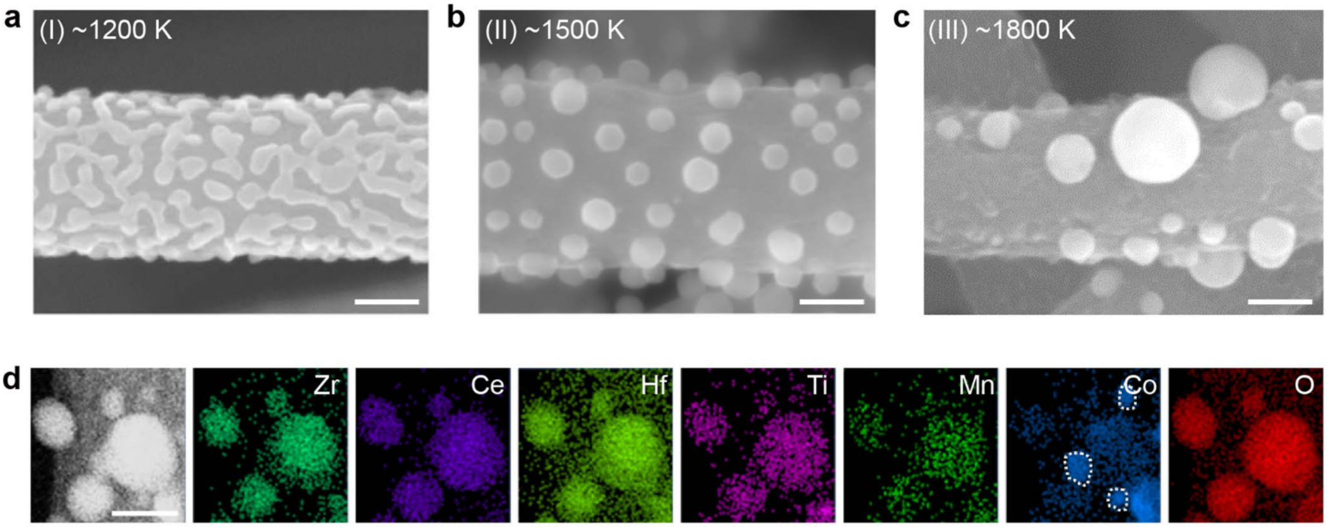

Extended Data Fig. 6 | Optimized synthesis temperature and high-temperature reduction. a, **b**, **c**, SEM images of (Zr,Ce,Hf,Ti,Mn,Co)O_{2-x} nanoparticles synthesized at low (I, ~1200 K) (**a**), optimized (II, ~1500 K) (**b**), and high (III, ~1800 K) (**c**) temperatures for 500 ms. Scale bar = 100 nm. **d**, Elemental mapping of (Zr,Ce,Hf,Ti,Mn,Co)O_{2-x} synthesized at 1800 K. Too high-temperature (1800 K) synthesis may lead to reduction of Co metals (phase separation) and particle overgrowth. Scale bar = 50 nm.

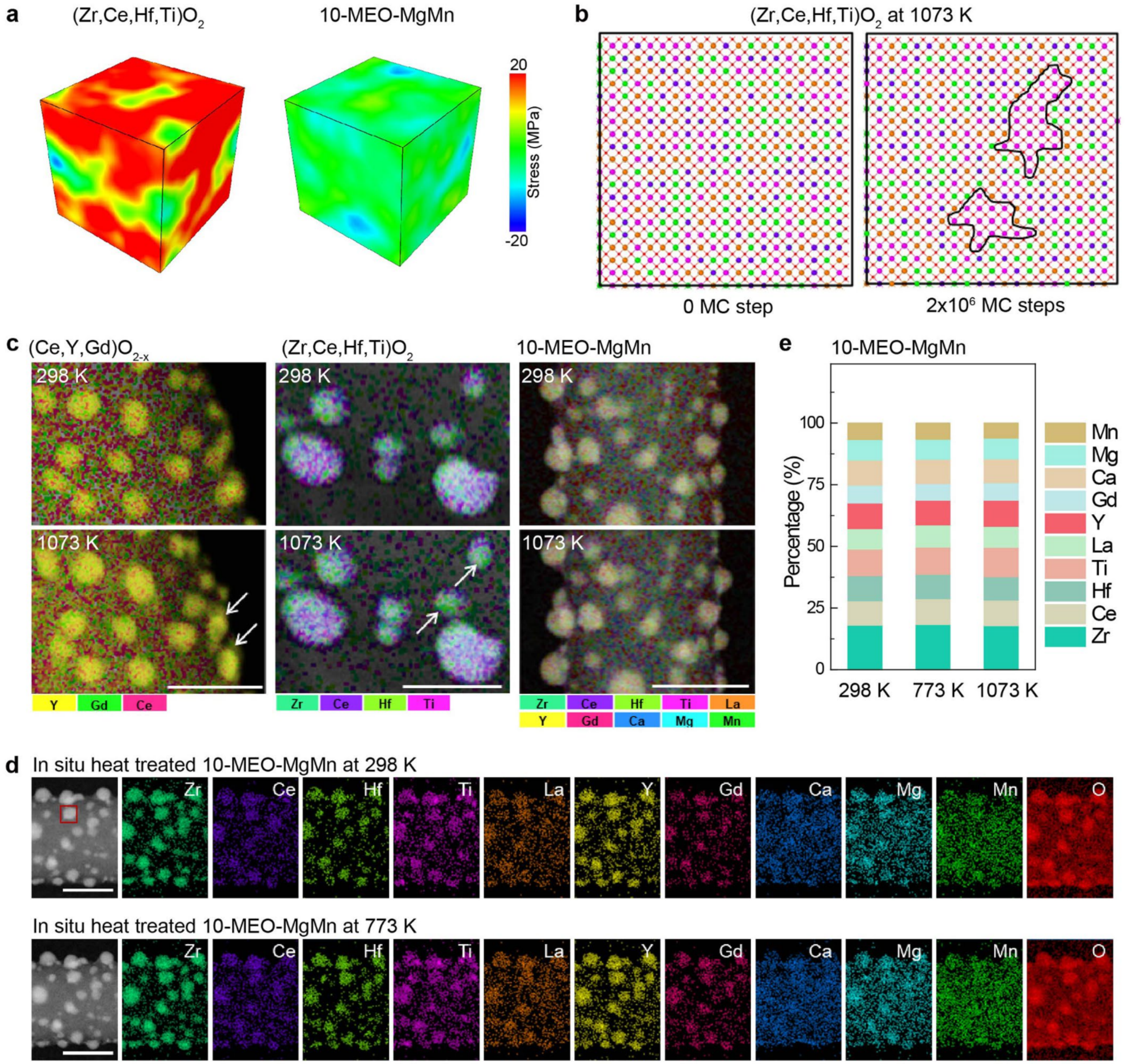

Extended Data Fig. 7 | The thermal stability of denary oxide nanoparticles. **a**, The microscale stress distribution for quaternary $(Zr,Ce,Hf,Ti)O_2$ and denary 10-MEO-MgMn. The 10-MEO-MgMn shows a more uniform stress distribution than the $(Zr,Ce,Hf,Ti)O_2$, suggesting a relatively more stable structure. **b**, The thermal stability (that is, after 2×10^6 Monte Carlo (MC) steps at 1073 K) for quaternary $(Zr,Ce,Hf,Ti)O_2$, which shows phase separation after thermal annealing at 1073 K. **c**, TEM elemental mapping of *in situ* heat-treated $(Ce,Y,Gd)O_{2-x}$, $(Zr,Ce,Hf,Ti)O_2$, and 10-MEO-MgMn nanoparticles. The denary oxide 10-MEO-MgMn nanoparticles remain almost the same after in situ annealing at 1073 K for 1 h, with little change in the particle size, dispersity, and elemental mixing, while $(Ce,Y,Gd)O_{2-x}$ and $(Zr,Ce,Hf,Ti)O_2$ show elemental segregation. Scale bar = 50 nm. **d**, The elemental mapping of 10-MEO-MgMn nanoparticles at 298 K and 773 K. Scale bar = 50 nm. **e**, The elemental concentration evolution in the 10-MEO-MgMn nanoparticles, derived from the single nanoparticle in the red box of Extended Data Fig. 7d. The composition ratio also remained similar during the *in situ* stability test.

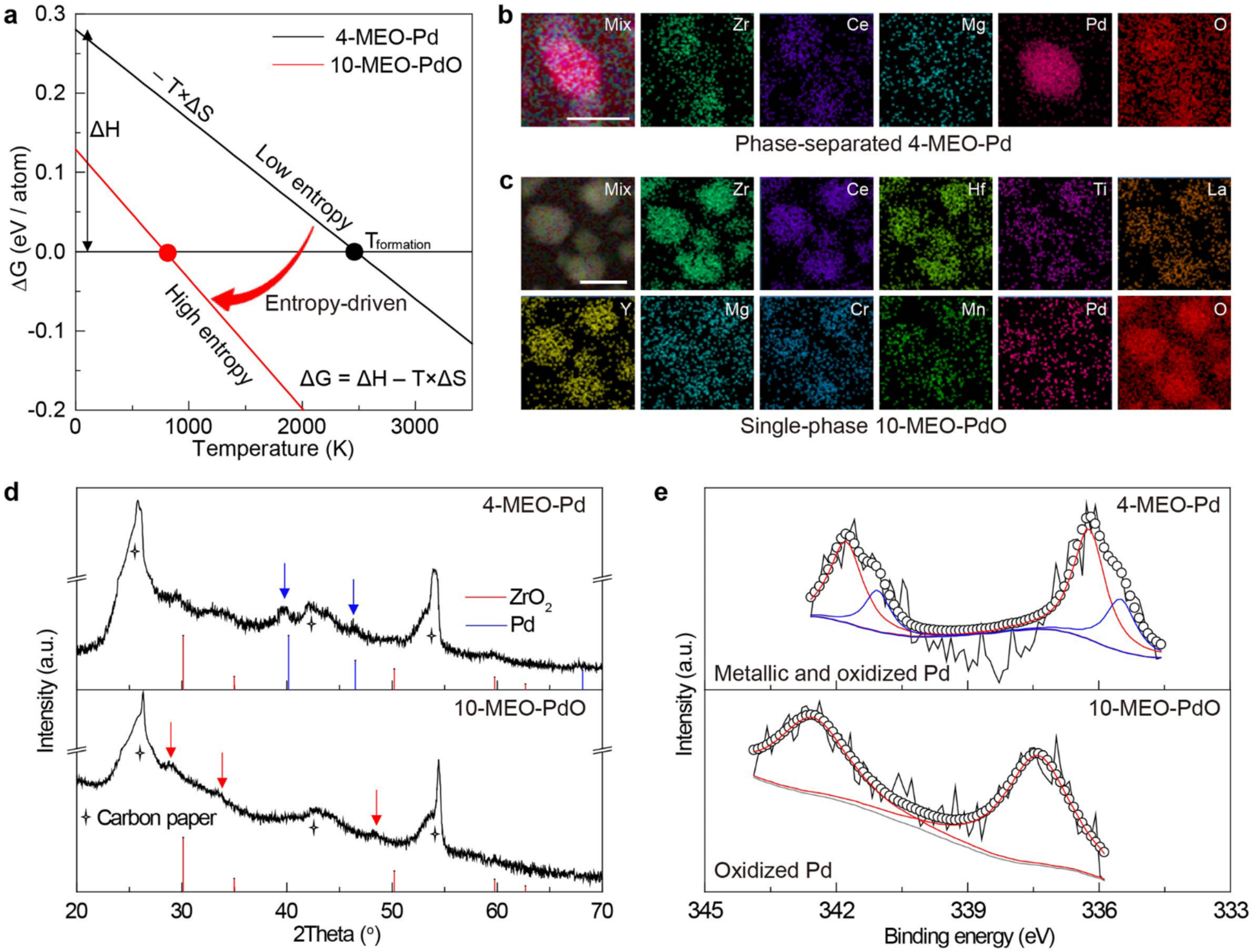

Extended Data Fig. 8 | Multi-element mixing to stabilize Pd in the oxidized state in 10-MEO-PdO nanoparticles. a, The temperature-dependence of the Gibbs free energy of (Zr, Ce)$_{0.6}$Mg$_{0.3}$Pd$_{0.1}$O$_x$ (4-MEO-Pd) and (Zr,Ce)$_{0.6}$(Hf,Ti,La,Y,Mg,Cr,Mn)$_{0.3}$Pd$_{0.1}$O$_{2-x}$ (10-MEO-PdO). The 10-MEO-PdO (a higher entropy) has a lower formation temperature (~790 K) at which the free energy of mixing becomes zero. However, the 4-MEO-Pd (with a lower entropy) cannot form single-phase fluorite structure below the temperature of ~2473 K. The calculated study demonstrates the entropy stabilization effect in the Pd-contained MEO systems. Thermodynamically, the increased mixing entropy and high-temperature synthesis provide a high entropic driving force ($\Delta G = \Delta H - T \times \Delta S$) which enables single-phase MEO formation and stabilization of PdO in the resulting MEOs. Kinetically, the PdO is trapped and stabilized in the denary MEO nanoparticles due to the high entropy structure with random mixing, lattice distortion, and slow kinetics. Detailed calculation models, parameters, and simulation process can be found in the Supplementary Methods. **b**, **c**, Elemental mapping of 4-MEO-Pd (**b**) (elemental segregation) and 10-MEO-PdO (**c**) (uniform mixing) nanoparticles. Scale bar = 10 nm. **d**, XRD of 4-MEO-Pd (phase separation) and 10-MEO-PdO (single phase) nanoparticles. **e**, XPS of the Pd element in 4-MEO-Pd (Metallic and oxidized Pd) and 10-MEO-PdO (Oxidized Pd). The evolution of Pd from a mixture phase (in the 4-element system) to a stable oxide PdO in the denary MEO (10-element system), demonstrating an entropy-driven mixing and stabilization of noble metal Pd.

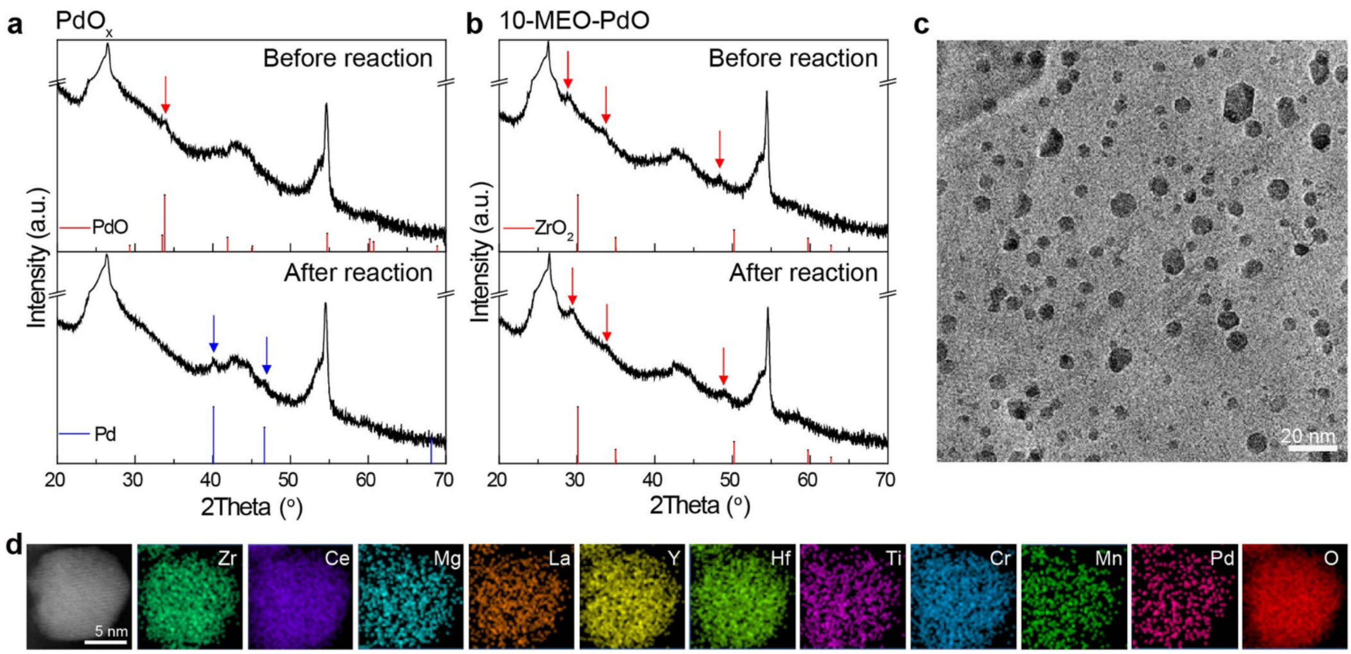

Extended Data Fig. 9 | Stability of the 10-MEO-PdO catalyst. **a**, XRD patterns before and after the methane combustion reaction for the control Pd sample synthesized by the traditional impregnation method, showing the PdO (indexed to PdO (PDF#43-1024)) was reduced to metallic Pd (indexed to Pd (PDF#46-1043)). **b**, XRD patterns before and after the methane combustion reaction for our 10-MEO-PdO (indexed to ZrO_2 (PDF#49-1642)) nanoparticles with excellent thermal stability. **c**, TEM image and **d**, elemental mapping of our 10-MEO-PdO nanoparticles after reaction, showing the uniform dispersion and mixing, without particle coarsening or elemental segregation.

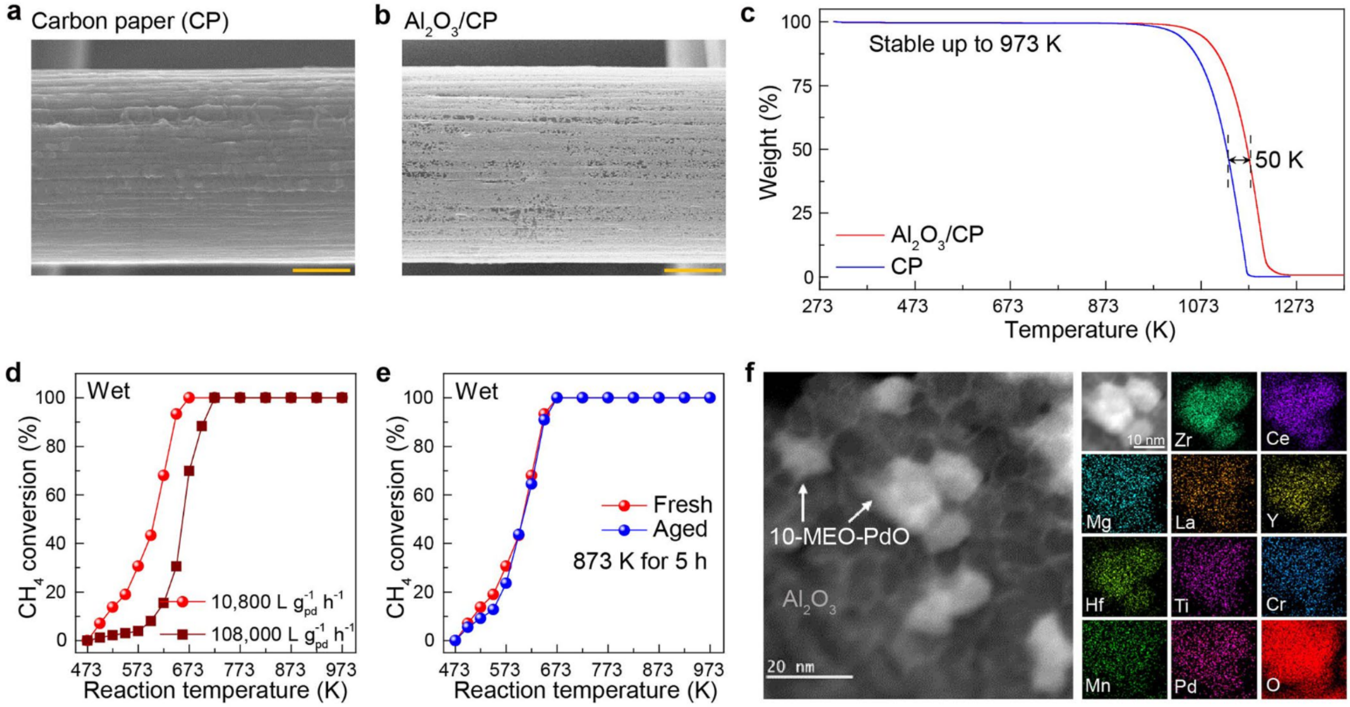

Extended Data Fig. 10 | The 10-MEO-PdO dispersed on the Al_2O_3-coated carbon paper for methane combustion performed under wet conditions. **a**, **b**, SEM images of carbon paper without (**a**) and with (**b**) Al_2O_3 coating. Scale bar = 2 µm. **c**, TGA data (performed in air atmosphere) of carbon paper (CP) without and with the Al_2O_3 coating. The Al_2O_3 coating increases the decomposition temperature of the substrate, which shows excellent stability up to 973 K. **d**, CH_4 conversion of 10-MEO-PdO on the Al_2O_3-coated carbon paper performed under wet conditions at different GHSVs. **e**, CH_4 conversion of 10-MEO-PdO on the Al_2O_3-coated carbon paper performed under wet conditions at the GHSV of 10,800 L g_{pd}^{-1} h^{-1} before and after annealing at 873 K for 5 h under the catalytic reaction condition, demonstrating the excellent stability of the catalyst under wet conditions at high temperatures. **f**, STEM image and elemental mapping of 10-MEO-PdO nanoparticles on the Al_2O_3-coated carbon paper after 100 hours of operation carried out under wet conditions, showing the uniform distribution and mixing of the nanoparticles, without coarsening or elemental segregation.